Universidad Carlos III de Madrid

Escuela Politécnica Superior

Modelling and optimisation of magnetic circuits for next generation Hall-effect thrusters

Bachelor Thesis

Bachelor in Aerospace Engineering

Author:

Francisco de Borja
De Saavedra García del Río

Tutor:

Daniel Pérez Grande

June 21st, 2017

Abstract

Within electric propulsion, Hall-effect thrusters are an attractive alternative to chemical propulsion for low-thrust applications. The applied magnetic field in Hall thrusters is a relevant part of the design process, on which studies are conducted for erosion reduction, among others.

The present thesis is focused on the magnetic topology of next generation Hall-effect thrusters. A magnetostatics simulation tool for axisymmetric problems is developed on the basis of the Finite Element Method Magnetics solver, with which it is possible to attain different topographies, as the so known as singular-point and, within Erosion Reduction Strategies (ERS), the magnetic shielding. In addition, the tool allows for the launching of several simulations in series (a batch), in which different parameters may be modified from one case to the next.

In the line of the development of magnetic circuits, a parametric study on coil design is performed, revealing the parameters necessary to fulfil geometric and electric current constraints on coils. The analysis allows for the design of a circuit feasible to be manufactured if properly translated from the axisymmetric model to a three-dimensional geometry, furthermore with the possibility of mass or power optimisation.

Finally, a scaling process on the basis of an existing device is performed to design a low-power Hall thruster, of which main design parameters, and, building on them, a suitable magnetic circuit, are obtained.

Contents

List of Figures

List of Tables

Chapter 1

Introduction

Electric propulsion is an irrefutably growing alternative to chemical rockets in the field of in-space propulsion. The increased efficiency and the rising availability of electrical power aboard spacecraft make electric propulsion a feasible and attractive choice for low-thrust applications. The appropriate design and simulation of the magnetic field is an essential piece for certain types of electric propulsion thrusters, and might eventually lead to a change of paradigm if sufficient power is attained on board (e.g. through the use of nuclear power sources).

The present thesis is focused on the modelling of magnetic topographies for next generation electric propulsion (EP), paying particular attention to Hall-effect thrusters (HETs). In addition, scaling laws will be analysed and a small HET will be scaled down from an existing thruster.

In this preliminary chapter, the reader will understand the basics of EP and HETs. Furthermore, the scope and objectives of the project will be addressed.

1.1 Electric Propulsion

Chemical propulsion has powered spacecraft since the beginning of astronautics. Nonetheless, the low efficiency and energy limit of combustion rockets triggered the search for alternative power sources.

Within non-chemical technologies, electric propulsion is a class of space propulsion that takes advantage of electric and/or magnetic fields to produce thrust. The outcome is a much higher mass efficiency and an extensive service life (in the range of tens of thousands of hours) in detriment of produced thrust, which is incomparable to that obtained through chemical means. The amount of thrust produced by an EP thruster is bounded by the available electric power on board of the spacecraft,

given that electric propulsion is power-limited, and not energy-limited as chemical propulsion is. Thence the traditional scheme of using chemical rockets for high-thrust applications and electric propulsion otherwise.

Throughout the 20$^{\text{th}}$ century, starting off with the SERT-1 in 1964 [5], electric propulsion has been studied in depth, leading to the use of hundreds of thrusters in different spacecraft. They have proven to outperform chemical propulsion regarding operating life and propellant usage for low-thrust applications, primarily space scientific missions (as EURECA [6], Deep Space 1 [7] or GOCE [8] among many others), and station-keeping of communications satellites, for instance from Telstar, Eutelsat and Deimos Imaging.

1.1.1 Rationale of electric thrusters

The performance of space propulsion systems is mainly assessed in terms of thrust and specific impulse. These parameters will be analysed for EP thrusters and compared to chemical propulsion systems.

From the formal definition of thrust

$$F = \dot{m} u_e \tag{1.1}$$

the specific impulse reads

$$I_{sp} = \frac{F}{\dot{m}_p g_0} = \frac{u_e}{g_0} \ [s] \tag{1.2}$$

where $\dot{m}$ is the mass flow exiting the thruster (coincident with propellant mass flow, $\dot{m}_p$), u_e is the exhaust velocity of the ions and g_0 is Earth's gravitational acceleration at standard mean sea level, which is included for historical reasons, giving specific impulse in seconds.

Whilst thrust requirements may depend on the characteristics of the mission, a high specific impulse is always a desirable feature in space propulsion. This is easily justified by the well-known Tsiolkovsky rocket equation

$$\frac{m_i}{m_f} = \exp\left(\frac{\Delta V}{I_{sp} g_0}\right) \tag{1.3}$$

where m_i is the initial (total) mass, m_f is the final (payload) mass, ΔV is the total velocity cost of the mission and the specific impulse is introduced in seconds. For a given ΔV, required by the mission, it is straightforward to notice that the required propellant mass decreases exponentially with the specific impulse. For this reason, the high specific impulse of EP thrusters provides them with a much better mass

efficiency than the chemical option. This is exemplified in Table 1.1, which collects, among other parameters, the typical specific impulse range for various thrusters.

The superior specific impulse of EP thrusters is given by the huge exhaust velocity attained. Conservation of energy for a single ion being accelerated through an electrostatic potential V gives

$$u_{e,ion} = \sqrt{\frac{2qV}{M}} \tag{1.4}$$

where q and M are the ion charge and mass, respectively. As an example, consider xenon as propellant, with an atomic mass of $M = 131.29\ u$, singly ionised (i.e. $q = e$) and being accelerated through a voltage drop of $V = 1500\ V$. Correspondingly, $u_e \approx 46950\ m/s$, assuming a uniform ion exhaust velocity. Thence, from (1.2), the resultant specific impulse would be $I_{sp} \approx 4790\ s$. Nonetheless, many complicated mechanisms and sources of inefficiency are present in current thrusters, limiting these figures to that shown in Table 1.1.

On the other hand, chemical propulsion is energy-limited so the exhaust velocity is bounded. In addition, the maximum achievable temperature in the combustion chamber is limited by the thermal endurance of the materials used, restricting further the exhaust velocity. Small bi-propellant chemical thrusters typically exhaust at $2500 - 3500\ m/s$, thence the order of magnitude of difference in I_{sp} between electric thrusters and the latter.

With regard to thrust, EP thrusters are limited by the electrical power that can be supplied to the system, being unable to compete with chemical propulsion for high-thrust operation. A simple expression for thrust in electric thrusters can be obtained from the product of ion mass flow and exhaust ion velocity. The former is related to the ion beam current, I_b, by

$$\dot{m}_{ion} = \frac{I_b M}{q} \tag{1.5}$$

Thence, assuming that the exhaust is fully ionised and that the contribution of electrons to thrust is negligible, eqs. (1.1), (1.4) and (1.5) give [4]

$$F = \sqrt{\frac{2M}{q}}\ I_b\ \sqrt{V} \tag{1.6}$$

As an illustration, considering singly-ionised xenon and a voltage of $V = 1500\ V$ as previously, the resultant thrust for a typical ion beam current of $I_b = 2\ A$ is $F \approx 127.8\ mN$. Again, this figure is merely theoretical; the actual thrust would

typically be smaller than 100 mN in these conditions.

As aforementioned, in reality, the resulting specific impulse and thrust of the previous hypothetical thruster would be smaller, given that the divergence of the exhaust and the presence of multiply-ionised species is not accounted for in the previous analyses. Besides, the presence of additional power-requiring elements that do not contribute to thrust produce a further reduction of thruster efficiency. In short, beam divergence, mass-utilisation efficiency and electrical efficiency degrade the performance (see [4] for further details on thruster efficiency).

Considering all the aforementioned, the advantage of EP is evident for long-range missions (i.e. requiring a large ΔV), allowing for a much greater payload mass fraction than chemical thrusters. The small thrust provided increases the duration, but prompt accomplishment is typically not a strong requirement in deep-space missions. As a matter of fact, the extended lifespan and low level of thrust of electric thrusters are a highly valuable asset for station-keeping and certain orbital manoeuvres, efficiently granting an accurate orbit control for long periods of time.

Nonetheless, it should be kept in mind that EP is currently not an option for high-thrust missions or manoeuvres. Furthermore, its operation is limited to in-space applications, given that electric thrusters can only work in vacuum conditions.

1.1.2 Classification of EP systems

Electric propulsion thrusters encompass any non-chemical device that provides thrust through electric and/or magnetic means. These systems can be broken down into three main types according to the source of acceleration of the propellant:

- Electrothermal: the gas is heated in the chamber by means of electric power. A nozzle located downstream expands the fluid and accelerates it towards the exit, providing thrust. Prominent within this category are the Resistojet and the Arcjet. The former relies on the flow of current through an electric resistance for the provision of thermal energy, whereas in the Arcjet a high voltage difference induces a high current arc through the gas to heat it up. Note that ionisation in the latter occurs weakly so that plasma effects are insignificant [4].

- Electrostatic: propellant ionisation is provoked to generate plasma and then accelerate it to high exhaust velocities by means of a cathode-anode pair induc-

ing a voltage difference. Notable devices included in this class of EP systems are Ion and Hall-effect thrusters. Although Ion thrusters feature the highest efficiency and specific impulse, Hall ones provide a larger thrust at a given power and entail less complexity.

- Electromagnetic: the propellant is ionised into plasma for Lorentz forces to accelerate it towards the exit. Noteworthy among these devices are the Pulsed Plasma Thruster (PPT) and the Magnetoplasmadynamic (MPD) thruster. The latter operate at very high powers to achieve high specific impulse, thence providing a higher thrust as compared to the previous devices.

A comparison of specific impulse and other parameters for the aforementioned thrusters with flight heritage is provided below.

Thruster	Specific impulse [s]	Input power [kW]	Efficiency range	Propellant
Cold gas	50-75	—	—	Various
Chemical (mono-propellant)	150-225	—	—	N_2H_4, H_2O_2
Chemical (bi-propellant)	300-450	—	—	Various
Resistojet	300	0.5-1	65-90	N_2H_4
Arcjet	500-600	0.9-2.2	25-45	N_2H_4
Ion thruster	2500-3600	0.4-4.3	40-80	Xenon
Hall thruster	1500-2000	1.5-4.5	35-60	Xenon
Pulsed plasma thruster	850-1200	< 0.2	7-13	Xenon

Table 1.1: Typical operating parameters of different types of thrusters. *Source: [4]*

1.1.3 Hall-effect thrusters

Classified as electrostatic or electromagnetic propulsion systems, HETs are a type of EP thruster that relies on both electric and magnetic fields to produce thrust. In order to explain the operating principles of the Hall plasma thruster, it is convenient to define its components in the first place. The typical annular configuration, which is schematically depicted in Fig. 1.1, consists mainly of the following:

- Propellant: heavy, neutral gas, typically xenon, which is converted into plasma, accelerated and exhausted to produce thrust.

- Discharge channel: (annular) region in which the propellant is ionised and through which the resulting plasma streams. The walls of the channel are typically covered, for protection, in a dielectric ceramic material, whose erosion determines the lifespan of the thruster.
- Hollow cathode: electron gun which discharges to the plasma and acts as the cathode of the electric circuit.
- Anode: counterpart of the latter. Besides, the propellant is injected into the discharge channel through small holes in it.
- Magnetic circuit: combination of elements generating the applied magnetic field.

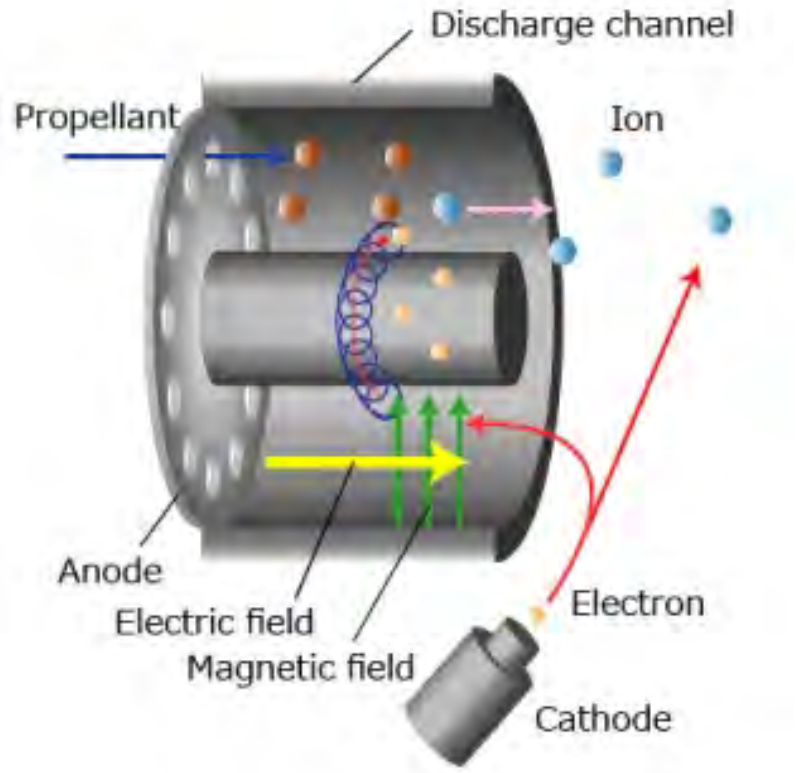

Figure 1.1: Basic components of a Hall-effect thruster. *Source: Komurasaki & Koizumi Laboratory, Department of Aeronautics and Astronautics, The University of Tokyo*

The working principle of the Hall thruster is to be explained now. The HET relies on two main mechanisms to operate. In the first place, the cathode gun fires electrons, which, under a potential bias provided by the power supply, ionise the propellant upon energetic collisions in their way towards the anode. On the other hand, the magnetic circuit imposes an essentially radial magnetic field of low

intensity, which is able to confine the electrons but has a negligible effect on the ions.

The superposition of the axial electric field — carried by the plasma itself and induced by the cathode-anode pair — and the applied radial magnetic field cause the electrons to suffer a so called ExB drift in the azimuthal direction, becoming trapped in a closed drift and generating a Hall current, after which the thruster is named. Thence, the magnetic field is responsible for impeding the motion of the electrons towards the anode, preventing the short-circuiting of the electric system and improving the ionisation efficiency, as the residence time of the electrons on their way from the cathode to the anode is greatly increased, allowing for more chances of ionising collisions to occur. On the other hand, the electric field is responsible for accelerating ions in the plasma axially towards the exit, generating thrust. The Lorentz force from the interaction between the beam current density and the magnetic field, known as JxB, is the coupling mechanism through which thrust is transmitted.

For the purpose of maintaining a neutral charge both in the spacecraft and in the jetted propellant cloud, a fraction of the electrons discharged through the cathode gun travels towards the exhaust, accompanying the ions and neutralizing the thrust beam.

Finally, it should be noted that the plasma-wall interaction is crucial in HETs, given that erosion and heat flux are determined by the energy of particles reaching the wall, which is affected by the plasma sheath, a boundary layer that appears at the walls of the discharge channel. In the end, the interaction with the walls is a source of inefficiency and is directly linked to the service life of the thruster.

A wrap-up of the different mechanisms involved in the operation of Hall thrusters is provided in Fig. 1.2.

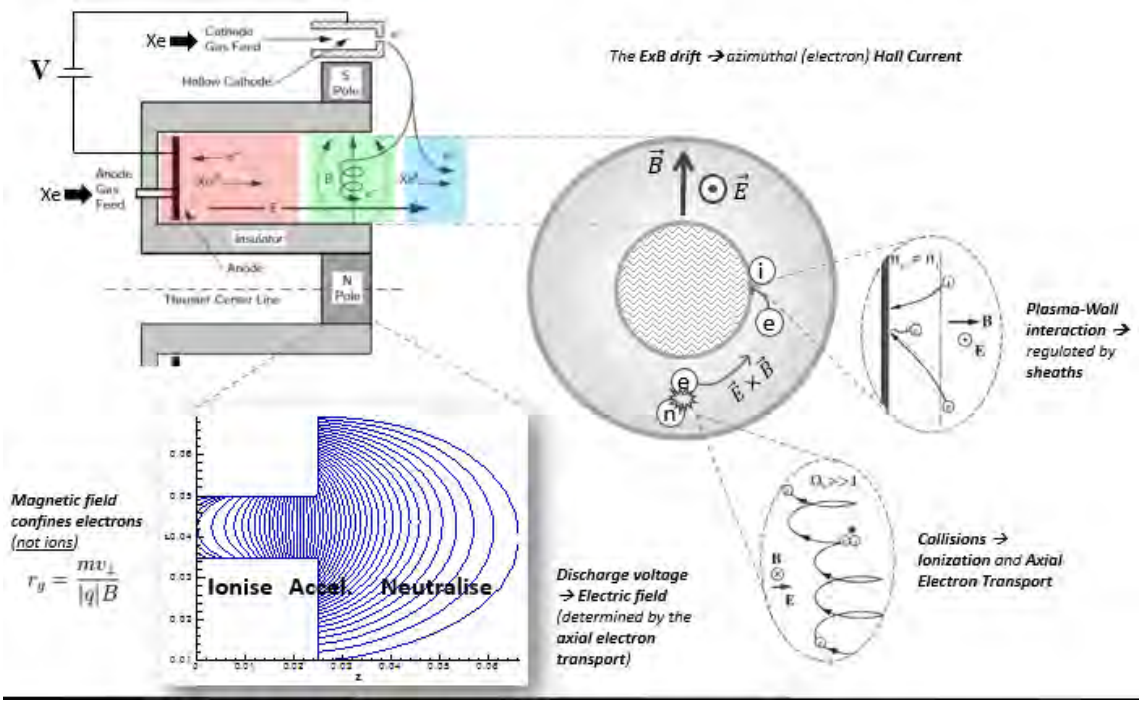

Figure 1.2: Schematic summary of HET operating principles. *Source: NOMADS - Advanced Simulation Tools for next generation Hall-Effect Plasma Thrusters, Daniel Pérez Grande, Space Propulsion and Plasmas research group, Universidad Carlos III de Madrid*

1.2 State of the art

Hall-effect thrusters are being increasingly used for telecommunications and scientific missions with medium-high ΔV.

The PPS® 1350-G is a 1.5 kW, high-I_{sp} Hall thruster designed for orbital transfer and satellite/spacecraft control developed by Safran Aircraft Engines (formerly Snecma). Apart from being the main propulsion source on ESA's SMART-1 (Fig. 1.3a) lunar probe, the PPS 1350-G thruster is used by Alphasat — the first satellite of the Alphabus platform developed by Airbus Defence and Space and Thales Alenia Space (Fig. 1.3b) — for north/south station-keeping [9].

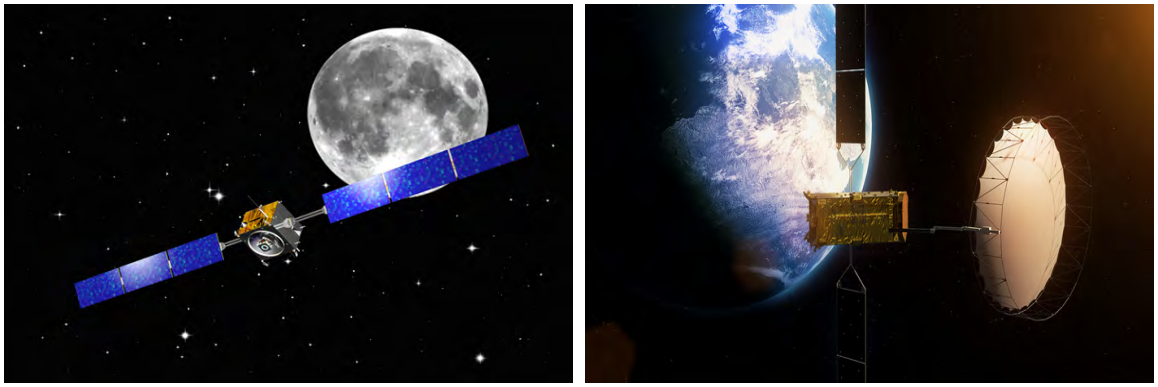

(a) Artist's impression of the SMART-1 mission. *Source: ESA*

(b) Artist's impression of the Alphasat. *Source: ESA*

Figure 1.3: Examples of spacecraft using the PPS® 1350-G Hall thruster

The future of communications satellites and deep-space missions certainly involves HETs. The PPS® 5000 is a 5 kW Hall thruster, currently under development by Safran, selected for the all-electric versions of the Eurostar 3000 (Airbus Defence and Space) and Spacebus (Thales Alenia Space), within ESA's Neosat project (next-generation satellite platforms) [10]. Many other future telecom satellites are planned to incorporate Hall thrusters for orbital positioning and/or station-keeping.

Regarding scientific space missions, within design trends for next-generation Hall thrusters, one of the main concerns is to extend the operating life. Within the so called Erosion Reduction Strategies (ERS), an approach is the magnetic shielding, which will be later explained and analysed in further detail. This tendency is exemplified by the 12.5 kW thruster HERMeS (Hall Effect Rocket with Magnetic Shielding) developed in collaboration by the NASA Glenn Research Center and the Jet Propulsion Laboratory to serve the Asteroid Redirect Mission (ARM), which has a nominal lifetime of 50,000 h and 3000 s specific impulse [11].

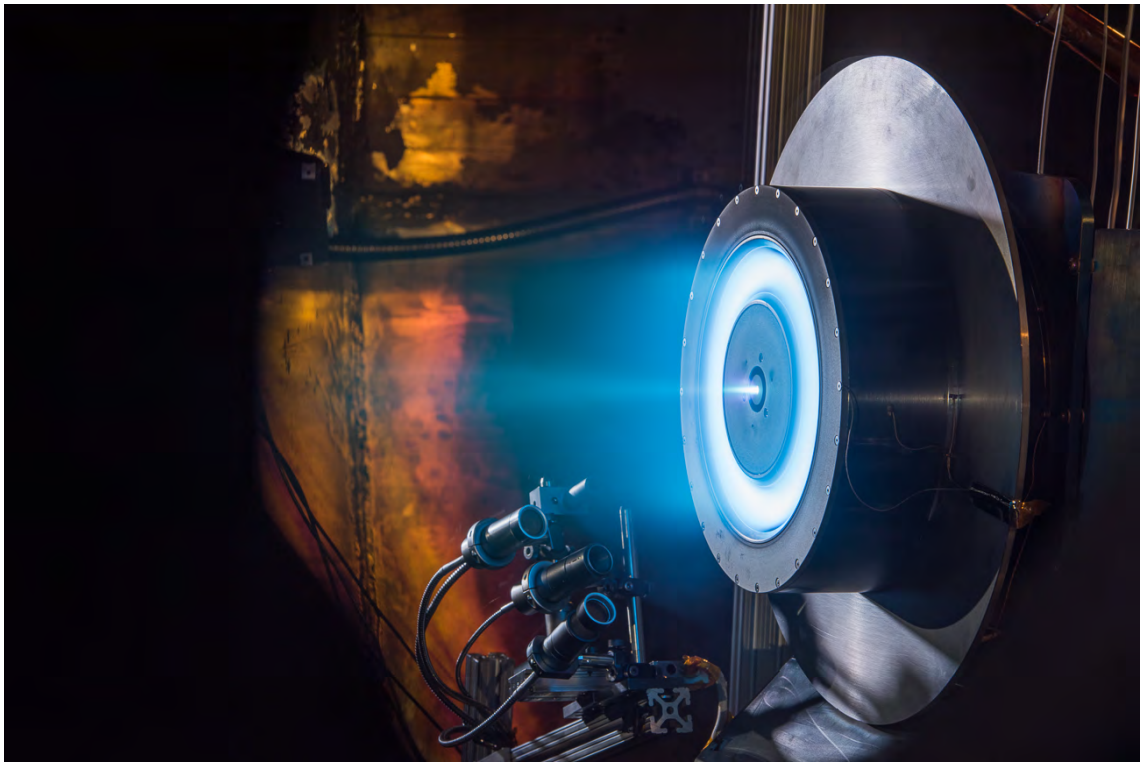

Figure 1.4: HERMeS prototype thruster being tested at NASA's Glenn Research Center. *Source: NASA*

The development of Hall thrusters is an ongoing activity, carried out by several groups of different institutions around the world. New challenges will be brought by the possibility of an increased available power on board of spacecraft, together with the research and experimentation on Hall-derived devices (nested Hall thruster, cusps thruster, cylindrical Hall thruster, etc.). These next-generation devices may have noteworthy advantages with respect to conventional Hall thrusters. The present project lies within the push towards the characterisation and improvement of the aforementioned thrusters, being framed in the CHEOPS European project, within Horizon 2020, and will help the Space Propulsion and Plasmas research group at UC3M in their contribution to the project.

1.3 Problem statement

The design of an EP plasma thruster is an intricate and iterative process. To attain the desired characteristics of this type of device, i.e. the required performance parameters, it is necessary to have an understanding of the physics of the plasma streaming through it, and utterly useful to have the capability of simulating it.

Design parameters in the plasma thruster problem include, fundamentally, the geometry of the thruster, the power input to the electric and magnetic circuits, the operating propellant mass flow and the applied magnetic field. The latter is intrinsic to the geometry of the magnetic circuit, which, in addition, practically determines the geometry of the entire thruster.

Plasma physics equations can be solved in the corresponding domain (the thruster discharge channel) once the previous data are known. Nonetheless, achieving the applied magnetic field that results in the adequate physics (i.e. those providing the required performance) is a complex issue, rendering it an inverse problem. In the end, the magnetic field is an input for the plasma physics to be solved, as outlined in Fig. 1.5. Furthermore, designing the magnetic circuit that generates the target field is not straightforward. Therefore, attaining the appropriate combination of elements is an iterative process, driven by engineering intuition and supported by an adequate magnetics simulation tool.

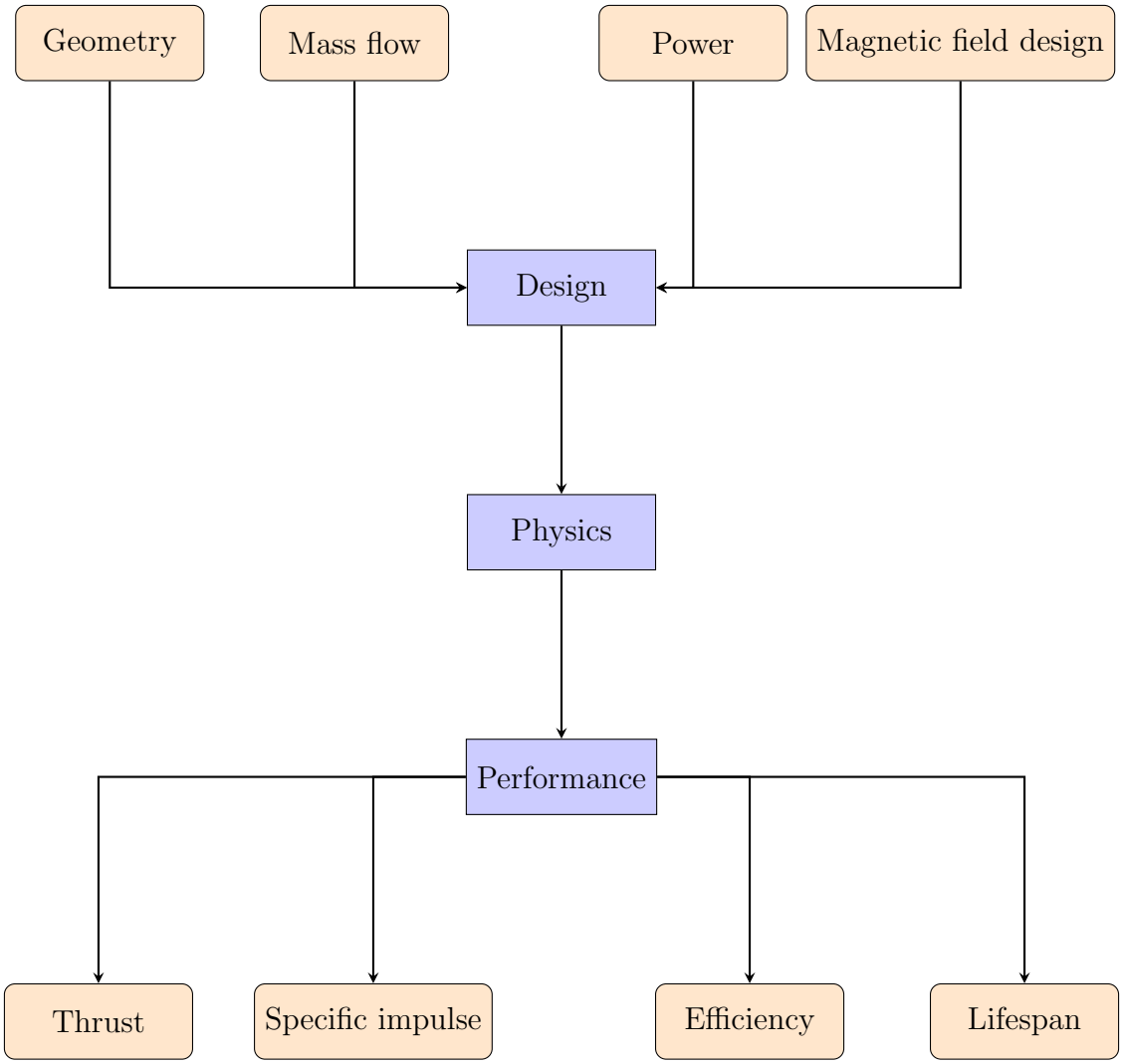

Figure 1.5: Ideal schematic of EP thruster development

1.4 Scope and objectives

The work performed for the present project involves the design and simulation of magnetic circuits for next-generation Hall-effect thrusters, encompassing an analysis of the elements available and their influence on the magnetic field, and, further, the attainment of magnetic topographies relevant for study. For this purpose, the author will develop a tool to implement and simulate various configurations.

Simultaneously, a study will be performed on the feasibility of coil parameters and their impact on mass and power required to provide a certain magnetic field.

Finally, the design of a low-power Hall thruster will be carried out with the use of scaling-down laws.

1.5 Regulatory framework

1.5.1 Related legislation

Electric thrusters, particularly Hall-effect devices, are ultimately devoted to space-related projects, in general for communications or scientific applications. In any mission, it is necessary to take outer-space law into account and to act in accordance with the different established rules and treaties.

With regard to the work developed by the author under the scope of the present thesis, there is no particular legislation applicable. Any possible use or future contribution of this project to a space-related activity must adhere to the space law, which will be introduced.

The main institution regulating space activities is the United Nations Office for Outer Space Affairs (UNOOSA). Space law addresses a wide variety of issues related to exploration, preservation of space and planets, liability for accidents, astronaut rescue, etc.

Nowadays, a relevant concern related to the preservation of the Earth environment is the removal of space debris. The space debris, defined by the UNOOSA as *all man-made objects, including fragments and elements thereof, in Earth orbit or re-entering the atmosphere, that are non-functional*, is a risk to spacecraft in Earth orbit, given that typically travel at velocities in the order of several kilometres per second. ST/SPACE/61 establishes guidelines towards the reduction of space debris, which include collision avoidance measures and limitation of long-term presence in LEO (low-Earth orbit), among others. All legislation can be consulted at [12].

1.6 Contents of this document

Heretofore, an introduction to electric propulsion and Hall thrusters has been provided, framing the work and scope of the thesis within them.

In the next chapter, the methods and software used to accomplish the aforementioned objectives will be described.

Afterwards, the progress towards the attainment of results will be detailed, and the latter will be discussed.

Finally, a socio-economic analysis will be provided before presenting conclusions of the work performed.

Chapter 2

Methods

As explained in Sec. 1.3, the use of an appropriate simulation code is fundamental to accomplish the aforementioned objectives. Throughout the present project, the author has developed a tool to implement magnetic circuits and obtain the corresponding magnetic field characteristics, providing the ability to simulate specific geometries and to do parametric studies by running batches of cases. The code, which is written in MATLAB®, encompasses the implementation of the problem and post-processing tasks, whereas pre-processing and the solution are accomplished by launching the open-source finite-element-method electromagnetics solver FEMM (Finite Element Method Magnetics) [13] through the MATLAB toolbox called OctaveFEMM, included in the FEMM source.

In the present chapter, the fundamentals of the Finite Element Method (FEM) will be covered first to introduce afterwards the solver used (FEMM). Finally, the tool developed by the author will be detailed, addressing its functionality and capabilities.

2.1 The Finite Element Method

Within many fields of Engineering and Physics, it is common to encounter problems that, due to the complexity of the domain studied or of the equations to be solved, are impractical or impossible to resolve analytically. In such cases, it is usually a better approach to break down the case into several but simpler small problems. This is the foundation of the Finite Element Method (FEM).

The FEM relies on the discretisation of the domain into simple, small parts — called elements — at whose junctions — the nodes — the problem is to be solved as a system of algebraic equations, yielding approximate values of the unknown

variables. Thence, with the use of interpolation, the parameters are known at any point in the studied space. Evidently, the precision of the method increases with the number of elements used and the order of interpolation.

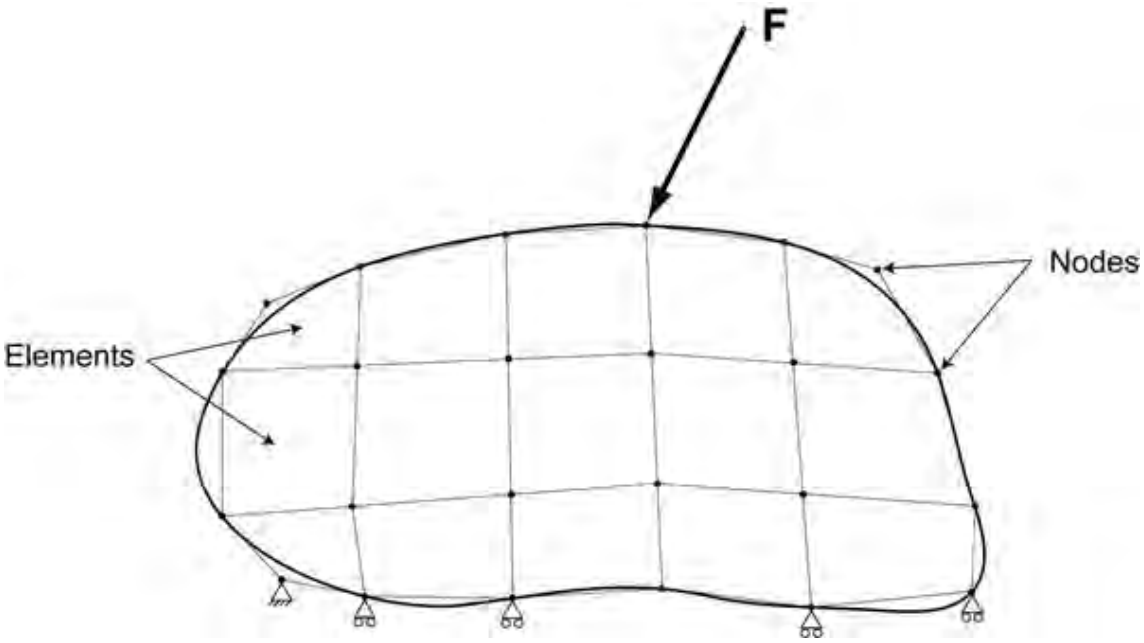

Figure 2.1: Schematic of a FEM mesh, formed by elements and nodes. *Source: [1]*

2.2 FEMM

Finite Element Method Magnetics is a numerical solver that takes advantage of the FEM to solve Maxwell's equations on planar two-dimensional and axisymmetric domains, dealing with magnetic, electrostatic, and current flow problems (heat flow is also addressed given its analogy with electrostatics). As far as the present project is concerned, only the magnetostatics part will be described, as FEMM is used within the author tool to solve the steady magnetic field generated by a certain circuit.

The general form of the well-known Maxwell's equations is

$$\nabla \cdot \boldsymbol{D} = \rho \tag{2.1}$$

$$\nabla \cdot \boldsymbol{B} = 0 \tag{2.2}$$

$$\nabla \times \boldsymbol{E} = -\frac{\partial \boldsymbol{B}}{\partial t} \tag{2.3}$$

$$\nabla \times \boldsymbol{H} = \boldsymbol{J} + \frac{\partial \boldsymbol{D}}{\partial t} \tag{2.4}$$

where ρ is the electric charge density, $\boldsymbol{J}$ is the electric current density, $\boldsymbol{D}$ is the displacement field, $\boldsymbol{E}$ is the electric field, $\boldsymbol{B}$ is the magnetic field and $\boldsymbol{H}$ is the magnetising field[(1)]. Considering no electric field and steady conditions, Maxwell's equations yield the magnetostatics problem

$$\nabla \cdot \boldsymbol{B} = 0 \tag{2.5}$$

$$\nabla \times \boldsymbol{H} = J \tag{2.6}$$

to which the constitutive relation between B and H fields, the magnetic permeability μ, must be added

$$B = \mu H \tag{2.7}$$

Finally, it should be noted that the permeability of non-linear materials is dependent on B

$$\mu = \frac{B}{H\left(B\right)} \tag{2.8}$$

The approach followed by Meeker [14] — FEMM's author — is to find a magnetic field that fulfils the former equations through the magnetic vector potential, $\boldsymbol{A}$, defined to satisfy

$$\boldsymbol{B} = \nabla \times \boldsymbol{A} \tag{2.9}$$

which allows to reduce the problem to a single, elliptic PDE

$$\nabla \times \left[\frac{1}{\mu\left(B\right)} \nabla \times \boldsymbol{A}\right] = \boldsymbol{J} \tag{2.10}$$

Retrieving B and H fields then reduces to differentiating the vector potential once it is known.

Boundary conditions available in FEMM include Dirichlet, Neumann, Robin, periodic and antiperiodic (see [14] for further details).

Given the specified problem, the solution (i.e. the vector potential distribution $\boldsymbol{A}$) is found through the discretisation of the domain into triangular elements and subsequent linear interpolation of the values at the vertices of the triangle.

[(1)] Given the absence of a convention in naming $\boldsymbol{B}$ and $\boldsymbol{H}$, they will be simply referred to as magnetic B-field and H-field, respectively.

2.3 Brief introduction to MATLAB

MATLAB® is a high-level-language numerical platform devoted to computational mathematics, being a registered trademark of The Mathworks Inc. Based on matrix objects, it is optimised for engineering and scientific problems. It contains plenty of toolboxes to interact with other software, built-in functions and documentation. MATLAB is used worldwide in different fields to analyse data, develop algorithms, create models, run simulations, manage graphics, etc.

2.4 Output format: HDF5

As detailed in Sec. 2.5.5, the results of the code can be exported in HDF5 format. HDF5 is a flexible and efficient file extension designed for input/output management.

The tool is adapted to the HYPHEN I/O standard through the use of HDF5 files to store data.

2.5 Tool developed by the author

In this section, the code used to design and simulate magnetic circuits will be described in detail, indicating which functions are developed or which are included in FEMM (but still used from MATLAB).

Consistently with the FEM, the attainment of the magnetic field involves pre-processing — including geometry generation, assignment of properties, boundary definition and meshing — and solving. As aforementioned, once the solution is retrieved, post-processing is performed within the author's code.

2.5.1 Pre-processing

All pre-processing activities are included in the MATLAB code and automatically implemented into the solver, which is launched through OctaveFEMM as explained previously.

Geometry

The shape and dimensions of the elements composing the circuit are defined in the first place. Given that the tool is prepared to deal only with 2D axisymmetric domains, the elements are typically represented as rectangles, but any closed shape can be managed.

Element properties

The components in the magnetic circuit can be classified into passive (ferromagnetic and permanent magnets) and active (coils). The main features to be assigned to the elements are the material and, in the case of a coil, the number of turns, N, and the current intensity, I, passing through it. Note that the magnetic field generated by a coil is dependent upon the effective coil current intensity, $I_{eff} = NI$.

Material properties and wire types included in FEMM can be used and assigned to elements directly from MATLAB. The solver includes an ample library containing different classes of permanent magnets, pure iron, steels, other metals, copper and aluminium wires, etc. Magnetic saturation is accounted for in FEMM and some non-linear magnetic materials are included. Furthermore, it allows for user-defined materials.

Finally, it should be noted that vacuum cannot be explicitly set in FEMM. Instead, air is used, given that its relative magnetic permeability is practically the unity ($\mu_{r,air} = 1.00000037$ [15]).

Boundary conditions

For the purpose of simulating Hall-effect thrusters, advantage will be taken from the axial symmetry of the typical configurations. Given the solving approach used by FEMM, a unique solution is obtained with no need of explicitly defining boundary conditions in axisymmetric problems. This is accomplished by enforcing null magnetic vector potential on the axis of symmetry ($\boldsymbol{A}_{r=0} = 0$), and, unless specified otherwise, imposing an Asymptotic Boundary Condition (ABC) at the limits of the domain, which closely approximates the unbounded solution for a sufficiently large boundary radius [14]. Nonetheless, for this to work, at least part of the boundary of the problem must lie on $r = 0$ as well.

The tool is designed to use BCs by default in the solver (those aforementioned). In any case, the boundaries of the problem must be defined. Thence, locating the

reference frame at the axis of symmetry of the thruster with the axial coordinate $z = 0$ at the exit of the discharge channel, the domain for the simulations is selected to be enclosed by a semicircle located at the origin of the reference frame with radius $5R_t$, being R_t the radial span of the thruster.

Meshing

FEMM includes a built-in mesher called Triangle, which creates a grid based on triangular elements. The mesh size cannot be directly specified, but, if not using the automatic mode, elements can be controlled through defining the maximum triangle side length that any element may have.

The code is arranged so that results are interpolated from the FEMM mesh to a user-defined results mesh. Note that a factor can be input to ensure that the elements in the Triangle mesh are smaller, for interpolation to be accurate. If the automatic Triangle mesher is not opted, the maximum FEMM element length will be defined as the minimum element length in the results mesh divided by the mentioned factor. To ensure appropriate results in the region of interest, this is applied to a zone around the thruster extending axially $-L_t \leq z \leq 2R_t$ (with $z = 0$ at the exit of the discharge channel) and radially $0 \leq r \leq 2R_t$, entailing a fine mesh as defined by the user. In the remaining vacuum (air) zone the automatic mesher is used, as illustrated in the example shown in Fig. 2.2.

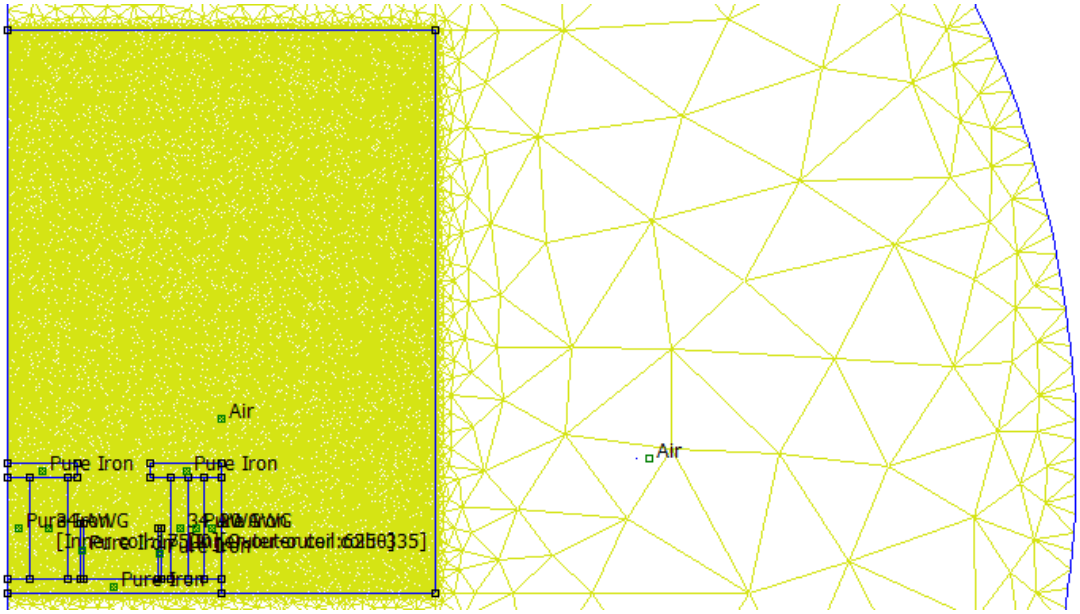

Figure 2.2: Mesh used in the solver, containing smaller elements in the region closer to the thruster and in the plasma plume to ensure accuracy where relevant. Note that coordinates are inverted with respect to the results mesh; here r is the horizontal axis and z the vertical one.

2.5.2 Solving

Given the permeability and current intensity distributions — introduced by the geometry and properties of the elements —, FEMM is able to solve eq. (2.10) through the Finite Element Method. The differentiation to retrieve the distributions of the axial and radial components of the magnetic field, $\boldsymbol{B_z}$ and $\boldsymbol{B_r}$ respectively, is directly performed by the solver. Furthermore, in case of using active magnetic elements (coils), it is possible to capture the current intensity (actually an input) and voltage (computed by FEMM) through each of the coils, which is fundamental to obtain the input power of the magnetic circuit, P_{mag}, a relevant parameter of the thruster.

2.5.3 Post-processing

The computation of relevant magnetic parameters is directly performed in MATLAB from the aforementioned results given by FEMM.

In the first place, the distribution of the modulus of the magnetic field (or magnetic field intensity) $|\boldsymbol{B}|$ can be directly obtained from the distributions of the axial

and radial components

$$|\boldsymbol{B}| = \sqrt{|\boldsymbol{B_z}|^2 + |\boldsymbol{B_r}|^2} \tag{2.11}$$

Secondly, attaining the distribution of the magnetic coordinates λ and σ — the magnetic stream function and magnetic potential, respectively —, is fundamental for generating Magnetic Field Aligned Meshes (MFAM), which are used to reduce numerical diffusion errors when integrating the physics of anisotropic plasma mediums (out of the scope of this project). In particular, the contours of the magnetic stream function are the streamlines of $\boldsymbol{B}$, which follow the local direction of the field and compose the magnetic topography of the thruster. Furthermore, the σ distribution provides the magnetic equipotential contours, which are normal to field streamlines, representing the direction perpendicular to the magnetic field.

Analogously to the fluid dynamics Stokes stream function in axisymmetric incompressible flows, the magnetic stream function in cylindrical coordinates is defined to fulfil Gauss' law for magnetism

$$\nabla \cdot \boldsymbol{B} = 0 \longrightarrow \frac{\partial \lambda}{\partial z} = rB_r \ ; \ \frac{\partial \lambda}{\partial r} = -rB_z \tag{2.12}$$

On the other hand, approximating the magnetic field as irrotational — which is a good approach if the magnetic field induced by the plasma in the discharge is small compared to the applied field, as typically occurs —, $\boldsymbol{B}$ can be defined in function of the gradient of a scalar, the magnetic potential. This is analogous to the potential flow theory in fluid dynamics

$$\nabla \times \boldsymbol{B} \approx 0 \longrightarrow \nabla\sigma = \boldsymbol{B} \longrightarrow \frac{\partial \sigma}{\partial z} = B_z \ ; \ \frac{\partial \sigma}{\partial r} = B_r \tag{2.13}$$

given that the curl of the gradient of a scalar function is always null, $\nabla \times (\nabla\sigma) = 0$.

With the aim of attaining the λ, σ distributions, the finite difference method (FDM) is applied within the (user-defined) results mesh, at whose nodes the axial and radial magnetic field are known from interpolation of the FEMM mesh. Given that their relevance lies on the contours, i.e. on the variation of magnitude between different points in space, it is possible to define arbitrary values at a certain node and integrate the variables in space from it. Thence, the values of λ and σ at node n are computed from the ones at the previous node, $n-1$, according to the finite difference scheme

$$\begin{aligned} \lambda_n &= \lambda_{n-1} + \Delta z \left.\frac{\partial \lambda}{\partial z}\right|_{n,n-1} + \Delta r \left.\frac{\partial \lambda}{\partial r}\right|_{n,n-1} \\ \sigma_n &= \sigma_{n-1} + \Delta z \left.\frac{\partial \sigma}{\partial z}\right|_{n,n-1} + \Delta r \left.\frac{\partial \sigma}{\partial r}\right|_{n,n-1} \end{aligned} \tag{2.14}$$

where $\Delta z = z_n - z_{n-1}$ and $\Delta r = r_n - r_{n-1}$, referring to the nodes in the results mesh. The finite difference derivatives are set as the average value of the variable between the node and its previous

$$\left.\frac{\partial f}{\partial x}\right|_{n,n-1} = \frac{f_n + f_{n-1}}{2} \tag{2.15}$$

representing f any of λ and σ, and x any of z and r. This is a first-order method, and is limited in accuracy by the relative size of the elements, being considered valid for the meshes to be implemented and the use it may be put to.

Considering the previous FDM scheme, one finally finds

$$\begin{aligned} \lambda_n = \lambda_{n-1} \; + \; (z_n - z_{n-1}) \; \frac{r_n B_{r,n} + r_{n-1} B_{r,n-1}}{2} \; - \\ - \; (r_n - r_{n-1}) \; \frac{r_n B_{z,n} + r_{n-1} B_{z,n-1}}{2} \end{aligned} \tag{2.16}$$

$$\begin{aligned} \sigma_n = \sigma_{n-1} \; + \; (z_n - z_{n-1}) \; \frac{B_{z,n} + B_{z,n-1}}{2} \; + \\ + \; (r_n - r_{n-1}) \; \frac{B_{r,n} + B_{r,n-1}}{2} \end{aligned}$$

In consistency with the aforementioned, $\lambda = 0$ and $\sigma = 0$ are arbitrarily assigned at the node closest to the mean radius of the discharge channel and with the minimum axial coordinate of the results mesh (the axially-innermost point). From this node, the variables are integrated along the entire mean line of the channel. Afterwards, the algorithm advances radially outwards and inwards in two separate processes to finally cover the complete domain. The integration method is schematically depicted in Fig. 2.3.

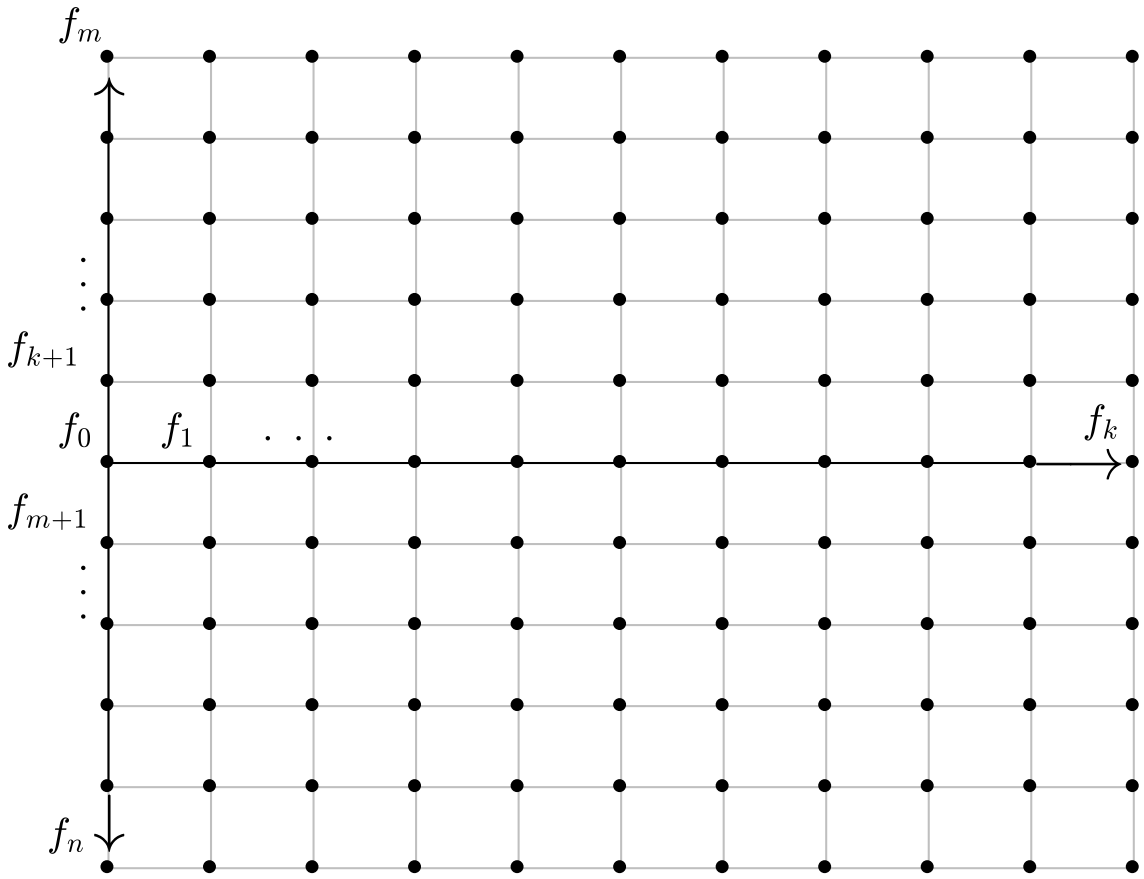

Figure 2.3: Schematic of the FDM algorithm used, where f represents the variable to be integrated (either λ or σ). First, the mean line is obtained, from f_0 to f_k. Next, integration follows radially, from f_0 to f_m and then from f_0 to f_n. The (radial) process is repeated for all nodes in the mean line, thence reaching the entire domain.

The rationale for using this algorithm, instead of simply integrating row by row or column by column for instance, is to avoid integration at nodes in the discharge channel — which is the region of most interest — from nodes within a ferromagnetic material, at which magnetic coordinates have higher gradients, due to larger values of the magnetic field intensity. Integration at the first node in a vacuum located right after a ferromagnetic region might lead to discontinuities in the magnetic coordinates within the domain, which are inadmissible for posterior meshing of the MFAM. By means of the aforementioned approach, since the algorithm advances from the mean line of the discharge channel, variables at all nodes in it will be prevented from having inadmissible errors.

Finally, it is possible to assess the cost of the magnetic characteristics obtained. Computing the input power to the magnetic circuit is straightforward from the current intensity and voltage of each coil, I_{coil} and V_{coil} respectively, given by the

solver. For n coils in the circuit, with $n \geq 1$

$$P_{mag} = \sum_{k=1}^{n} I_{coil,k} V_{coil,k} \tag{2.17}$$

2.5.4 Functionality and capabilities of the tool

The author will aid the Space Propulsion and Plasmas team at Universidad Carlos III de Madrid (UC3M) in their research, providing the team with a flexible tool by means of which they can obtain the topography and magnetic characteristics of any type of thruster, not only of HETs. Thence, the code developed, explained in the previous sections, is able to deal with configurations different than those of a typical annular Hall thruster. Nonetheless, the functionality of the tool is geometrically limited to axisymmetric domains.

Furthermore, the tool will work along with the so called HYPHEN (HYbrid Plasma-thruster Holistic-simulation ENvironment), a platform developed by the research group which is devoted to the simulation of the plasma discharge in the near plume of electromagnetic thrusters.

The code is structured in order that the user can set a reference case, from which various simulations may be launched. In the former, the user defines the geometry of the discharge channel and all the elements composing the magnetic circuit to be modelled, including all parameters required. On the basis of the reference case, it is then possible to modify specific properties of different elements and simulate the new particular case, with no need of defining an entire magnetic circuit again.

The manipulation of certain parameters differing from the reference case allows for launching a series of simulations — a batch of cases — automatically. The author's tool is prepared to run two different types of sequences:

- Simultaneous: the user defines a vector for each property of each element to be changed, containing the values to be updated (all vectors must have equal length). Every new case in the batch is generated from the modification of the corresponding parameters following the sequence specified in their vectors. In other words, it is possible to modify any number of properties of any number of elements at the same time in each simulation, so that the total number of cases in the batch will be determined exclusively by the length of the mentioned vectors.

- Progressive: similarly, a vector with the new values of each parameter are defined by the user, but equal length is not a requirement. In this sequence, cases are generated following the order in which the vectors are introduced, implementing one new modification at a time, thence advancing element by element and property by property within each of the former. The last value of each parameter modified is therefore kept for subsequent cases in the batch.

As an illustration, consider that the user desires to modify parameters a and b with respect to a reference case already implemented (with a_{ref}, b_{ref}). Then, different values for each parameter may be given, with modification vectors $\boldsymbol{a} = \{a_1, a_2, ..., a_m\}$ and $\boldsymbol{b} = \{b_1, b_2, ..., b_n\}$. If the simultaneous batch option is opted, in which case it is necessary that $m = n$, then n cases will be simulated automatically in series. Every case k — with $k = 1, 2, ..., n$—, will differ from the reference case both in that $a = a_k$ and $b = b_k$ (instead of $a = a_{ref}$ and $b = b_{ref}$).

On the other hand, if a progressive batch is commanded, the sequence will consist of $m + n$ cases. In the first m, every case k — with $k = 1, 2, ..., m$ —, will diverge from the reference case only regarding the first parameter, that is $a = a_k$ instead of $a = a_{ref}$. Afterwards, in the remaining n simulations, every case l — with $l = m, m + 1, ..., m + n$ —, will differ in the second parameter, i.e. $b = b_k$ instead of $b = b_{ref}$, in addition to maintaining the last change in the first one ($a = a_m$) for all l cases.

2.5.5 Code I/O

Outputs provided and inputs required by the tool are collected in Table 2.1 and Table 2.2, respectively.

Output	**Details**
Geometry figure	Illustration of the elements composing the magnetic circuit
Magnetic field intensity, $\|\boldsymbol{B}\|$	- Contours figure - Distribution (values at nodes in results mesh) in HDF5 file (optional)
Magnetic stream function, $\boldsymbol{\lambda}$	- Contours figure - Distribution (values at nodes in results mesh) in HDF5 file (optional)
Magnetic potential, $\boldsymbol{\sigma}$	- Contours figure - Distribution (values at nodes in results mesh) in HDF5 file (optional)
Power requirement	- Electric power needed by each coil - Total power input, P_{mag}

Table 2.1: Outputs of the tool developed by the author

Input	**Details**
Reference case	- Channel geometry - Elements (geometry and properties)
Particular case (single or batch)	- Channel modifications - Element modifications
Results mesh limits	$\{z_{min}, z_{max}, r_{min}, r_{max}\}$
Triangle automatic mesher	Yes / No
Results mesh size (number of elements)	$\{n_z, n_r\}$
Solver mesh — results mesh factor	$f = \frac{l_{min,results}}{l_{max,FEMM}}$
Number of λ streamlines	n_{strl}
Number of $\|B\|$, σ contours	n_{cont}
Case name	Label used in naming output files
Write output files (figures and HDF5)	Yes/No
Output figures file format	.png, .epsc, etc.

Table 2.2: Inputs of the tool developed by the author

Chapter 3

Study on magnetostatics of Hall-effect thrusters

With the tool developed, the author is capable of modelling different circuits and simulate the corresponding magnetic characteristics. In this chapter, results corresponding to the objectives described in Sec. 1.4 will be presented and discussed.

3.1 Magnetic elements

The magnetic circuit in the typical annular configuration of HETs consists of the components schematically depicted in Fig. 3.1.

The inner and outer coils are responsible for generating the magnetic field. On the other hand, internal and external trim coils are used to manage in a further controlled way the magnetic topography of the thruster.

The ferromagnetic casing of the thruster provides guidance to the magnetic streamlines and encloses the discharge channel. It is normally composed of inner front pole, outer front pole, inner core, outer flux guide and back pole. In particular, the front poles are important to attain a mainly radial magnetic field in the discharge.

Finally, ferromagnetic screens (inner and outer) provide shielding to the discharge channel, effectively reducing the field intensity and axially curving the streamlines inside. This will become apparent when dealing with magnetic shielding topographies [16] in Sec. 3.6.

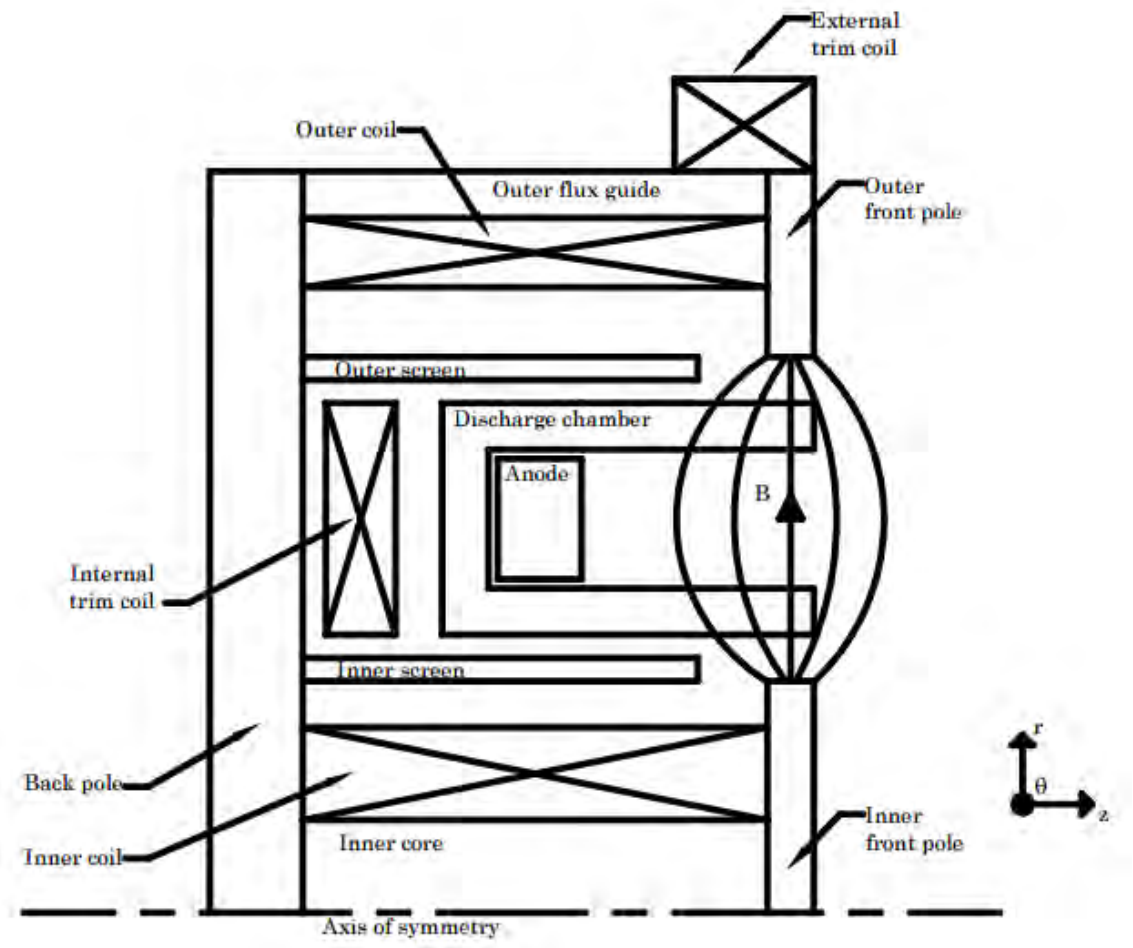

Figure 3.1: Cross-sectional schematic of typical magnetic elements in a Hall thruster. *Source: [2]*

3.2 Pre-reference case (virtual coils)

For the purpose of performing different simulations, it is convenient to build on the basis of a reference magnetic circuit, as explained in Sec. 2.5.4. The fundamental magnetic topography — over which modifications will be made to achieve new fields — is sought to be similar to that of the SPT-100 thruster, i.e. eminently radial at the channel and with a maximum magnetic field intensity of $|\boldsymbol{B}|_{max} \approx 250\ G = 0.025\ T$ in the plasma discharge [17].

To attain the geometry and properties of the magnetic circuit producing the mentioned characteristics, it was necessary to carry out several simulations and work on a trial-and-error basis. It should be noted that whether active elements (coils) are actually feasible to be built and used is not yet taken into consideration

(see Sec. 3.3), for which they will be denoted as "virtual". Furthermore, to model the effect of the (non-annular) outer coils, which are typically four in a HET, a single annular outer coil will be used, matching the axial symmetry of the problem.

The resulting model is shown in Fig. 3.2, in which the geometry of the circuit and relevant magnetic characteristics are illustrated.

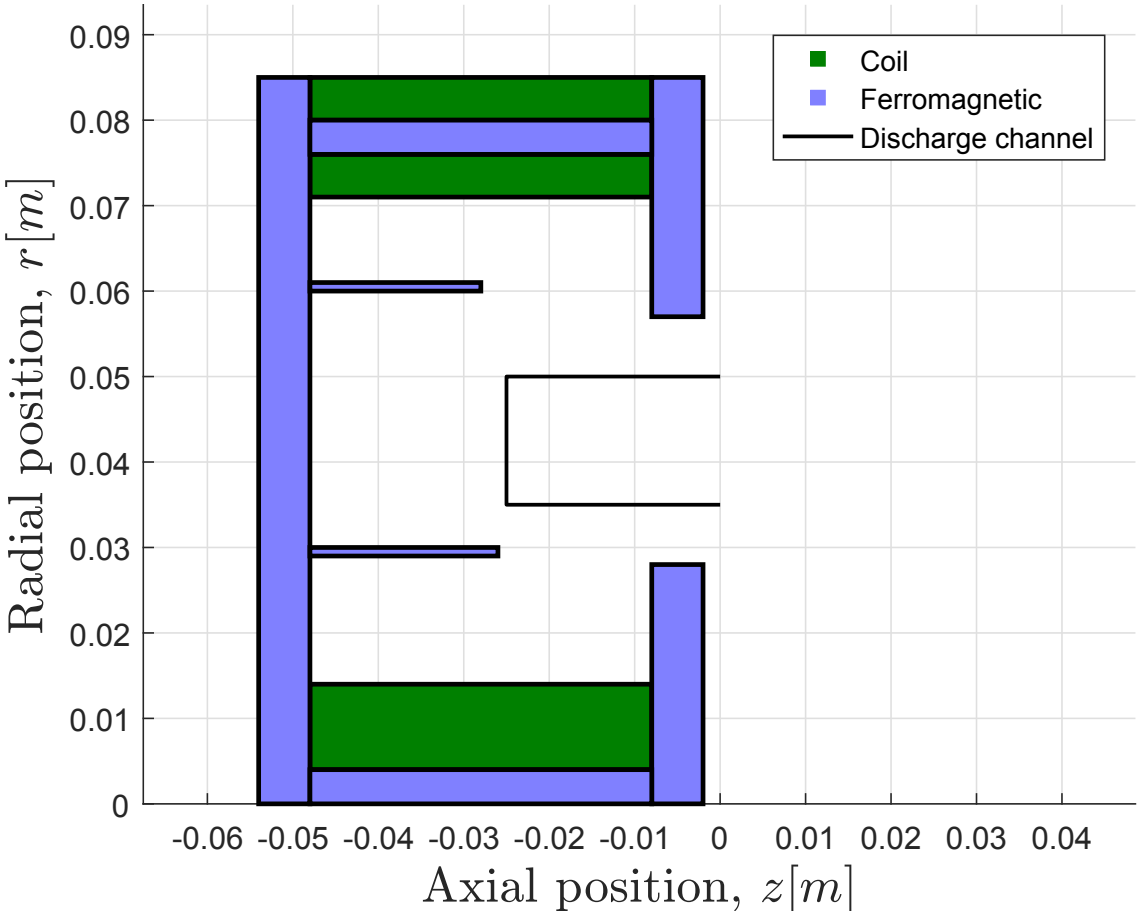

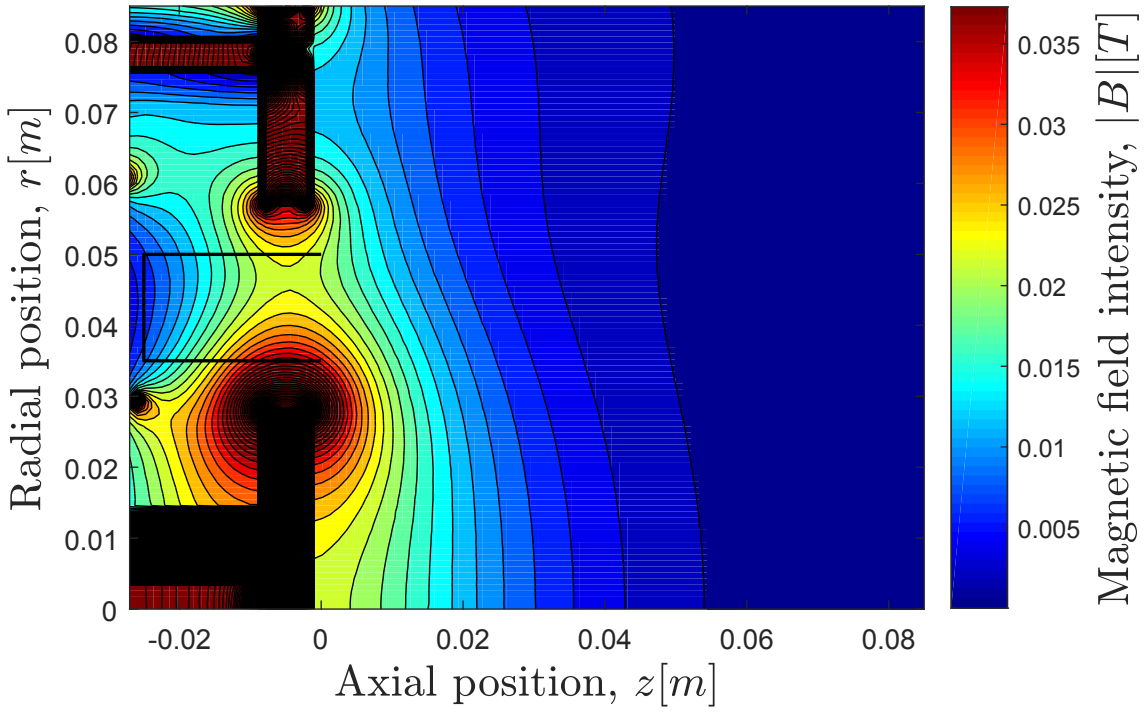

(b) Magnetic field intensity

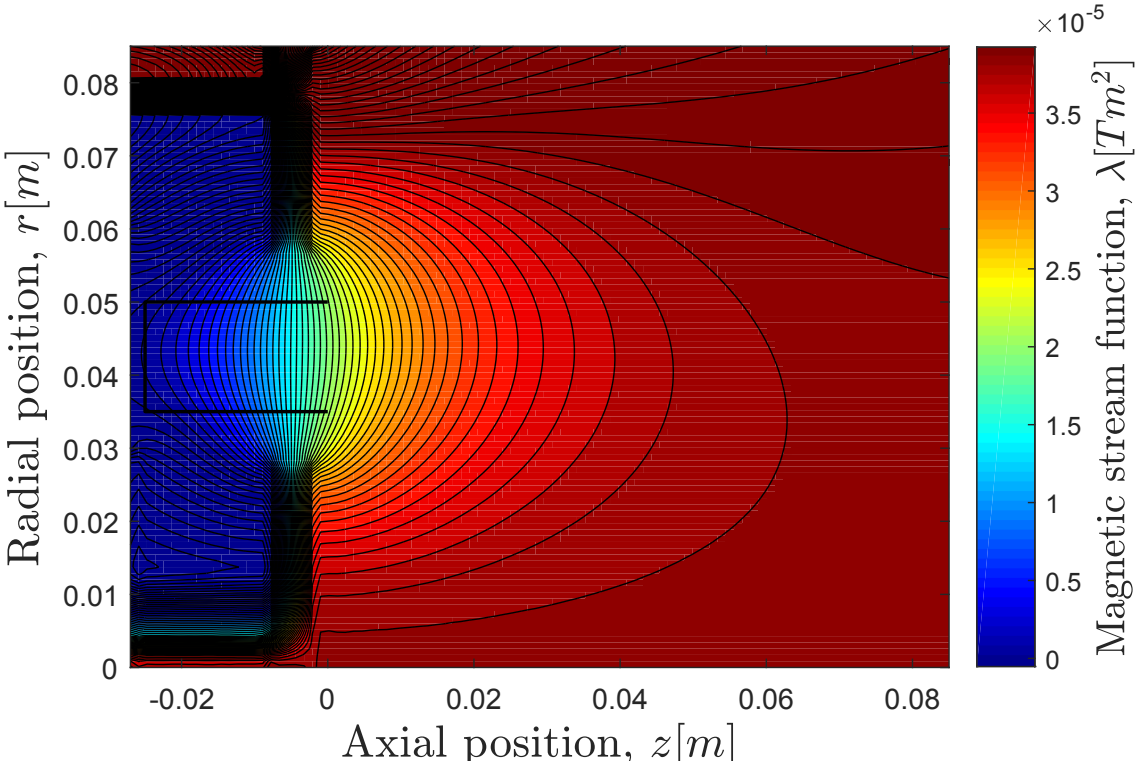

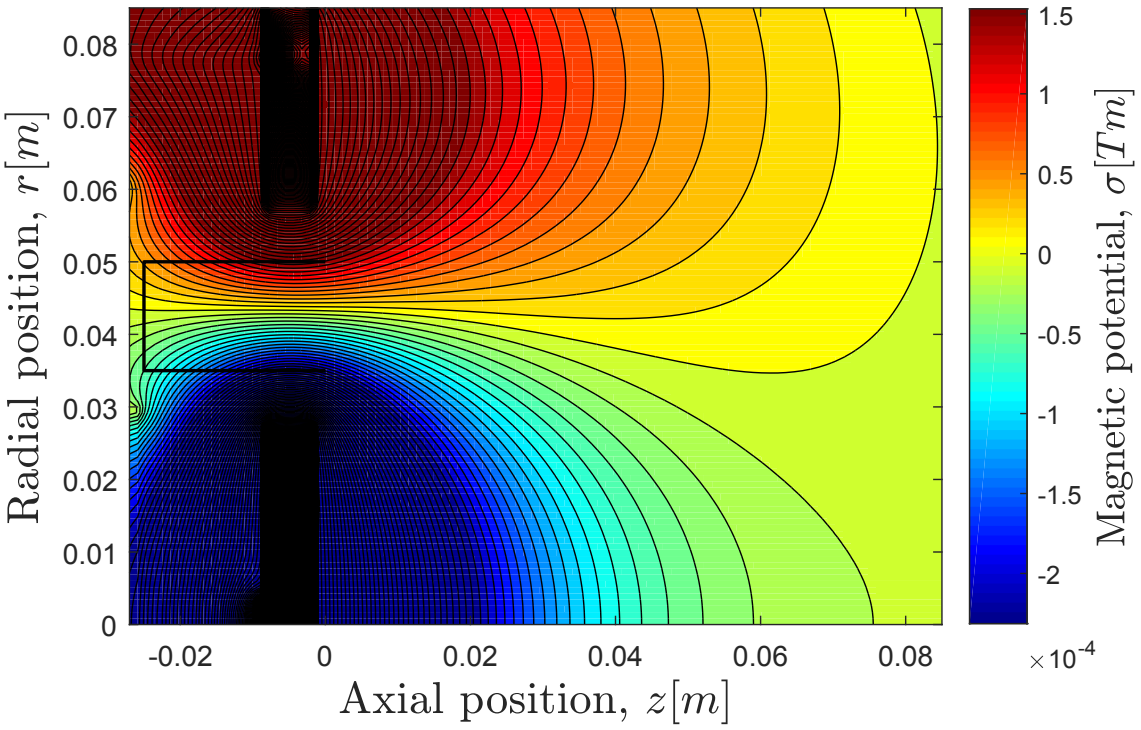

(d) Magnetic potential

Figure 3.2: Pre-reference case with virtual coils

The effective coil current intensity, NI, is the parameter that, for given geometry, yields a certain magnetic field. Therefore, if coil feasibility is disregarded, current intensity and number of wire turns are irrelevant provided their product is the adequate.

To obtain the previous case, a current of 1 A is used for all active elements, and the number of turns of each is adjusted as necessary to produce the desired field. Then, it should be noted that the coils' number of turns are infeasible given their geometry. In other words, a real wire with the number of turns required would not fit in the cross-sectional area of the coils in Fig. 3.2a. As an example, the inner coil in the case above is formed with a magnet wire 1.02 mm in diameter wrapped around 23500 times, thence occupying an azimuthal section of ≈ 24000 mm^2 (actually greater due to unideal wire packing) whereas the modelled cross-sectional area is 400 mm^2. Still, the simulation is possible counting on the fact that FEMM is able to model any coil, regardless of the number of turns, by using equivalent distributions.

With the aim of achieving a meaningful (and further realistic) reference case, a parametric study of coil design will be performed. Given that the previous case is impractical towards a design and manufacturing process, a detailed description of geometry and properties of all elements in the circuit will be given only for the adequate reference case, which is to be developed after the coil analysis.

3.3 Coil design

The fundamental objective of the study is to find the appropriate parameters that a coil must have to satisfy geometric, mass, power and magnetic field intensity requirements.

3.3.1 General guidelines

In the first place, the cross-sectional (azimuthal) area of the coil, which will be denoted $\bar{A}$, must accommodate the entire wrapping, with wire diameter d, apart from fitting in the space available in the thruster. Therefore, in a coil with axial span L and radial span D, each wire turn would ideally occupy a section area d^2, as illustrated in Fig. 3.3.

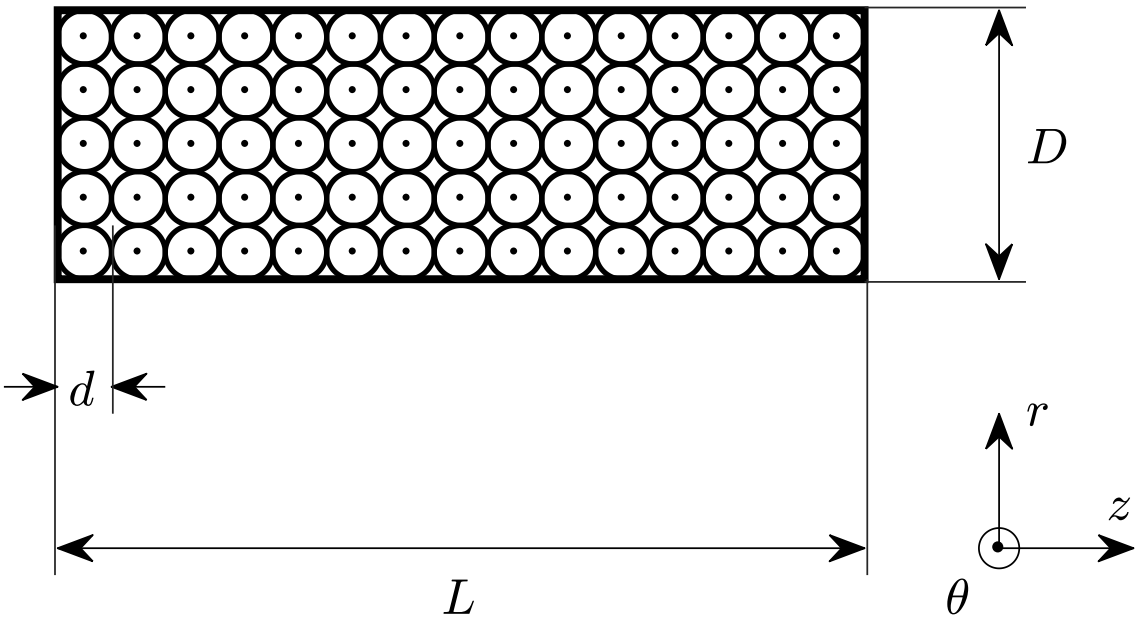

Figure 3.3: Schematic of ideal wire wrapping in the azimuthal section of a coil

Nonetheless, as the wire circles around the core of the coil, it requires extra axial spacing. Introducing a global packing factor f — evidently with $f < 1$ — that accounts both for the winding and the extra diameter of the conductor wire from the outer insulation, the number of turns N fitting in the cross section of the coil fulfils

$$\bar{A} = LD = \frac{1}{f} N d^2 \tag{3.1}$$

In the second place, wire "ampacity", i.e. the maximum electric current intensity to be carried with no immediate or progressive degradation, is to be taken into account.

The American Wire Gauge system will be used for convenience. Cables are identified with a number, the gauge (AWG), which determines their diameter through the following formula [3]

$$d = 0.127 \cdot 92^{(36-AWG)/39} \ [mm] \tag{3.2}$$

which yields that a decrease of 6 in gauge entails essentially doubling the wire diameter. Note that the outer insulation is not included in the former, but is taken into account through the global packing factor f.

Wire ampacity is broadly documented for the AWG system. Considering copper as conductor, plastic insulation and a solid wire (i.e. not stranded), the maximum

current intensity I_{max} to be carried in function of wire diameter d is depicted in Fig. 3.4 [3].

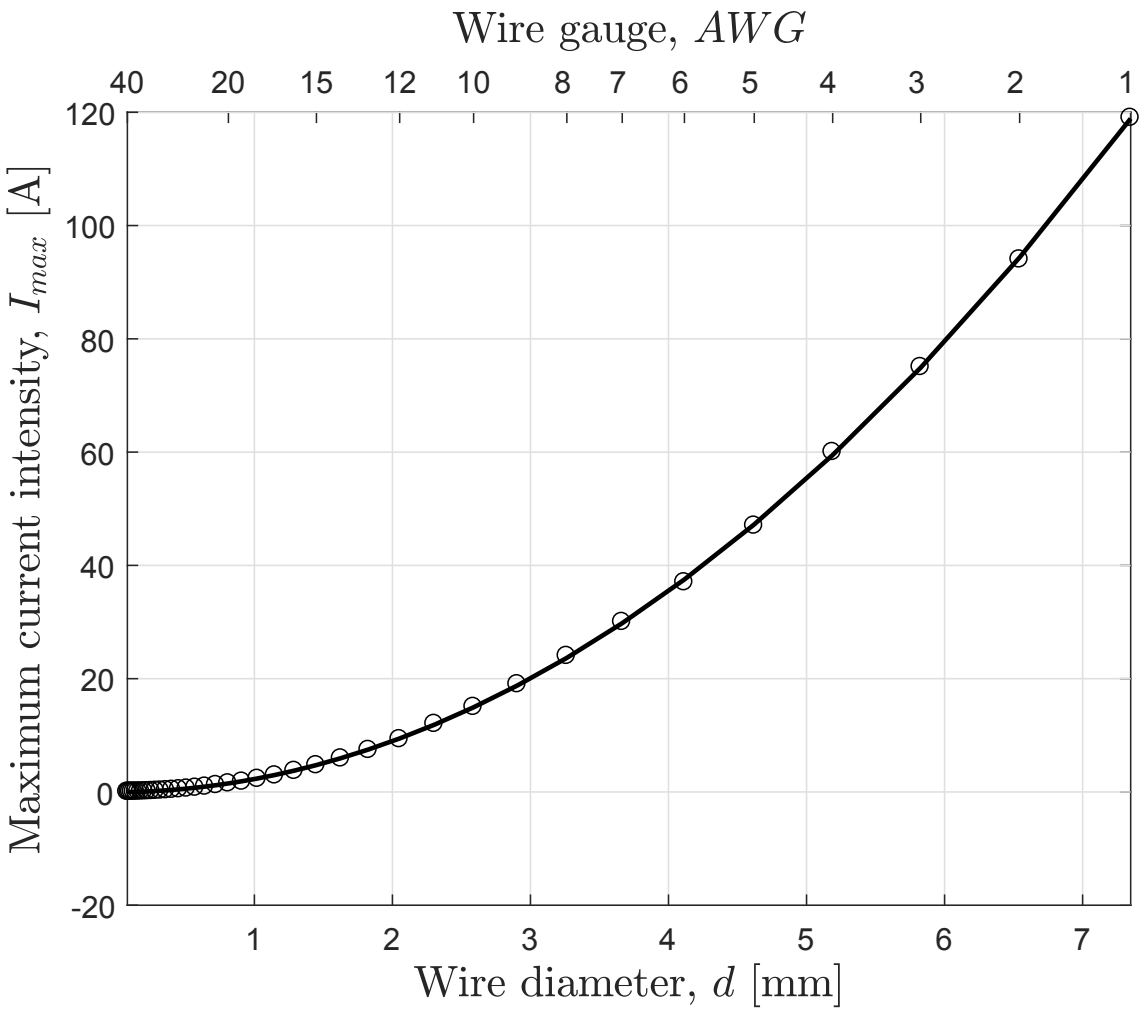

Figure 3.4: AWG wire ampacity for power transmission. *Source: [3]*

From the figure above, $I_{max} \propto d^2$ is inferred by least squares fitting, which is consistent with the fact that maximum current intensity is connected to heat flow in the wire, which involves the cross-sectional area ($\propto d^2$).

It should be noted that the data above corresponds to power transmission at an ambient temperature of 30 °C. In the end, ampacity depends on many factors, thence the reason behind considering power transmission data, which is strongly conservative, to allow for differences between the above data and the actual operating conditions.

Mass efficiency is a fundamental parameter to be considered. The impact of wire diameter and number of turns on the weight of the coil is also relevant to analyse.

The mass of the wire in the coil can be found from the material density, ρ

$$m_{wire} = \rho L_{wire} A_{wire} \tag{3.3}$$

where the total length of the wire is approximated by $L_{wire} \approx 2\pi R_m N$, being R_m the mean radius of the coil, and $A_{wire} = \frac{\pi}{4} d^2$ is the cross-sectional area of the wire.

Finally, as in any engineering design process, the cost must be assessed and minimised as much as possible. With regard to the coils in a magnetic circuit, the power input P_{mag} is the parameter representing expense, and is fully determined by the intensity passing through them and their characteristics.

The electric resistance of the wire R_{wire} reads

$$R_{wire} = \frac{L_{wire}}{\sigma A_{wire}} \tag{3.4}$$

where σ is the electrical conductivity and, again, $L_{wire} \approx 2\pi R_m N$, for a coil with N turns and mean radius R_m. Therefore, the power required by a single coil is

$$P = R_{wire} I^2 \approx \frac{8 R_m N}{\sigma d^2} I^2 \tag{3.5}$$

The previous analysis is valid for any wire application. Henceforth, the analysis will be particularised for the development of HET magnetic coils.

3.3.2 Parametric study for coils in a Hall thruster magnetic circuit

Consider a coil to be formed by a wire with conductivity σ, with minimum radius r_{min}, spanning a distance L axially and with the possibility of extending radially up to a position r_{max}. Whilst the former parameter depends upon the wire material, the other are given by the main dimensions of the thruster and the ferromagnetic components. As a matter of fact, L will typically be the distance from the back pole to the (either inner or outer) front pole and the limits $\{r_{min}, r_{max}\}$ will be determined by the geometry of the inner core or outer flux guide and by the position of the magnetic screens or the discharge channel itself in the absence of the former.

Furthermore, to attain a certain magnetic field, the effective coil current intensity $I_{eff} = NI$ is necessarily fixed. Thence, the product of number of turns and amperage (NI) becomes a constant in the analysis for a given element geometry.

The purpose of the study is, therefore, to find the combination of wire diameter, number of turns and current intensity input $\{d, N, I\}$ fulfilling wire accommodation in the coil section and maximum ampacity, in addition to minimising required power or wire mass.

For each wire diameter in the AWG series it is possible to determine the minimum radial span (as imposed by wire fitting), the wire mass and the power used in function of the number of turns. The former is found from eq. (3.1)

$$D_{min}\left(d, N\right) = \frac{1}{fL} d^2 N \tag{3.6}$$

where it is necessary that $D_{min} \leq D \leq r_{max} - r_{min}$ for the coil to fit in the available space in the thruster and to accommodate all the wire.

The wire mass is a function of cable diameter and number of turns

$$m_{wire} \approx \frac{\pi^2}{2} \rho R_m d^2 N \tag{3.7}$$

On the other hand, coil power can be expressed uniquely in function of d and N by means of introducing the effective current intensity NI in eq. (3.5)

$$P\left(d, N\right) \approx \frac{8 R_m \left(NI\right)^2}{\sigma d^2} \frac{1}{N} \tag{3.8}$$

where $R_m = r_{min} + D_{min}/2$. This is a relevant result. The dependency $P \propto 1/N$ indicates that it is desirable to use a high number of turns as far as cost is concerned, which may be applicable to any coil design process. It should be noted that a radial span greater than D_{min} can be selected, so that the actual coil power and wire mass would be higher; the minimum is used for closing the analysis.

Finally, the range of number of turns feasible for each wire diameter is defined to fulfil the aforementioned requirements. The minimum is determined from the maximum ampacity of the wire

$$N_{min}\left(d\right) = \frac{NI}{I_{max}\left(d\right)} \tag{3.9}$$

whereas the maximum is imposed by the space available for the coil in the thruster

$$N_{max}\left(d\right) = fL\left(r_{max} - r_{min}\right) \frac{1}{d^2} \tag{3.10}$$

Note that the previous analysis will be applied to any magnetic circuit included in the present thesis, thus implementing feasible coils in any case.

3.4 Reference case

It is now possible to apply the parametric study to attain an adequate reference case, with coils feasible to be manufactured.

The data of the three coils in the former circuit required for the analysis are summarised in Table 3.1. A winding factor of $f = 0.8$ will be assumed henceforth in any coil design. Furthermore, electrical conductivity should be accounted for. Considering gauges 10-36 of AWG copper wire (since these are the only wires from the AWG series included in FEMM) operating at an assumed temperature of 500 K, the conductivity is $\sigma = 32.36 \cdot 10^6\ S/m$ [18]. The estimation is based upon tested coil temperatures in an SPT-100 ML thruster at a plasma discharge of 300 W, which are around 490 K for the inner coil and around 470 K for the external ones [19], thence being slightly conservative. This value will be used in all cases. Finally, copper density needs to be considered, $\rho = 8960\ kg/m^3$.

Note that the appropriate design will be shown only for the inner coil, which is the most critical given its huge effective current intensity. However, the process is actually applied to all coils in order to achieve a feasible reference case.

Coil	Parameter	Value
(Virtual) inner	Axial span, L [mm]	40
	Radial span, D [mm]	10
	Minimum radial position, r_{min} [mm]	4
	Maximum radial position, r_{max} [mm]	27
	Effective current intensity, NI [A]	23500
	Wire gauge (diameter), AWG (d [mm])	18 (1.02)
(Virtual) inner-outer	Axial span, L [mm]	40
	Radial span, D [mm]	5
	Minimum radial position, r_{min} [mm]	73
	Maximum radial position, r_{max} [mm]	78
	Effective current intensity, NI [A]	300
	Wire gauge (diameter), AWG (d [mm])	18 (1.02)
(Virtual) outer-outer	Axial span, L [mm]	40
	Radial span, D [mm]	5
	Minimum radial position, r_{min} [mm]	82
	Maximum radial position, r_{max} [mm]	85
	Effective current intensity, NI [A]	625
	Wire gauge (diameter), AWG (d [mm])	18 (1.02)

Table 3.1: Coil parameters in virtual reference case

The analysis of the inner coil as described in Sec. 3.3.2 leads to the conclusion that it is not possible to design it to fulfil the requirements with the specified NI. The reason behind this is that the maximum ampacity constraint (3.9) imposes a minimum winding N_{min} which is larger than the maximum number of turns N_{max} fitting in the coil (3.10) for any wire diameter. This is clearly observed in Fig. 3.5, in which restrictions on number of turns against wire gauge are represented.

Therefore, in other words, it is found that the combination of parameters used (those of the inner coil in Table 3.1) is infeasible, given that maximum ampacity

and wire accommodation constraints cannot be accomplished simultaneously given

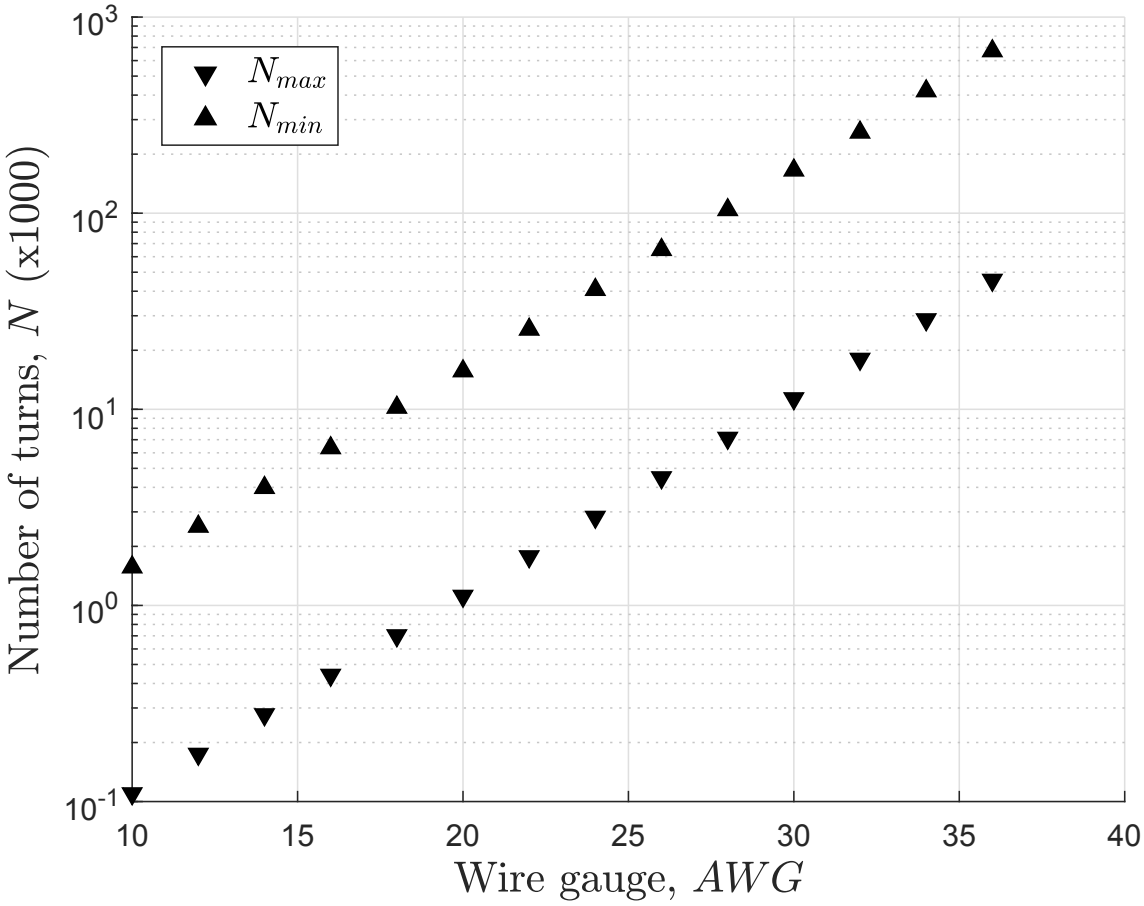

Figure 3.5: Maximum and minimum number of turns in function of wire gauge for the (virtual) inner coil with $NI = 23500\ A$

From the analysis, it is determined that, with the aim of attaining a reference case with feasible-to-build coils, it is necessary to reduce the effective current intensity. This parameter is obtained through the magnetostatic simulation process previously performed, reaching a certain value as needed to produce the desired field.

The magnetic characteristics required for the reference case are shown in Fig. 3.2. Diminishing NI of the inner coil alongside no other modification will clearly reduce the field intensity $|B|$ and deform the magnetic streamlines. Therefore, the solution will consist in extending radially the inner (ferromagnetic) core and the coil itself at the same time to make up for the drop in effective current intensity. Through this approach, increasing the outer radius of the ferromagnetic part from 4 to 9 mm and the radial span of the coil from 10 to 15 mm, it is possible to scale the parameter down from 23,500 to only $NI = 500$, a 97.9% reduction. The new geometry is shown in Fig. 3.6.

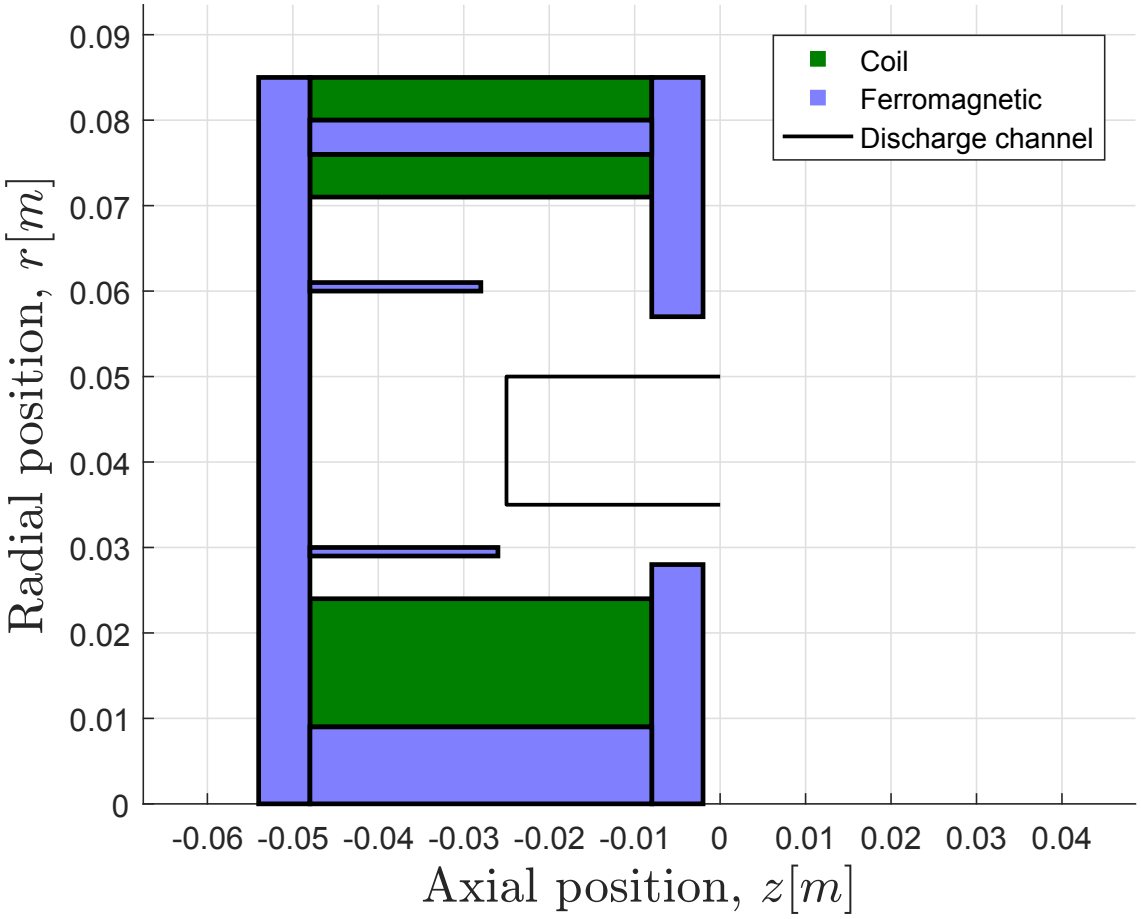

Figure 3.6: Pre-reference case geometry with virtual coils (inner core and inner coil modified toward feasibility)

The previous case is accomplished using still AWG 18 wires, with no regard to coil feasibility. However, it should be noticed that only the effective current intensity matters as far as the resulting magnetic field is concerned, rendering the simulation valid for any combination of the variables $\{d, N, I\}$ as long as the former remains unchanged. The new data of the inner coil appears in Table 3.2 (as aforementioned, the analysis will be shown only for the inner coil, although the definitive reference case is achieved after the study of all coils).

Coil	Parameter	Value
Inner	Axial span, L [mm]	40
	Radial span, D [mm]	15
	Minimum radial position, r_{min} [mm]	9
	Maximum radial position, r_{max} [mm]	27
	Effective current intensity, NI [A]	500

Table 3.2: Inner coil parameters after effective current intensity reduction

On account of the previous decrease in NI, it is possible to repeat the parametric study for the coils with meaningful results. With regard to the inner coil, the analysis results in Fig. 3.8. Note that winding constraints (3.9), (3.10) can be fulfilled now at the same time, as demonstrated in Fig. 3.7. The diagrams obtained allow for the selection of a design point (the adequate combination of coil parameters $\{d, N, I\}$), accomplishing all requirements and rendering the coil feasible to be manufactured and implemented into a real magnetic circuit.

Note that the range of input power in the diagram (Fig. 3.8c) is considerably narrow, so that cost minimisation is not a strong requirement. By inspection of Fig. 3.8a, deciding on the AWG 34 wire, the number of turns is conservatively selected for the minimum radial span to be roughly 1 mm smaller than the value used in the simulation (15 mm as shown in Table 3.2), therefore fulfilling $D > D_{min}$. In other words, the coil is opted to be designed with

$$AWG = 34\,(d = 0.16\ mm)\ \ ;\ \ N = 17500$$

for which

$$D = 15\,mm > D_{min} \approx 14\,mm\ ;\ I = \frac{500}{17500} = 0.0286\,A\ ;\ m_{wire} \approx 0.318\,kg\ ;\ P \approx 2.2\,W$$

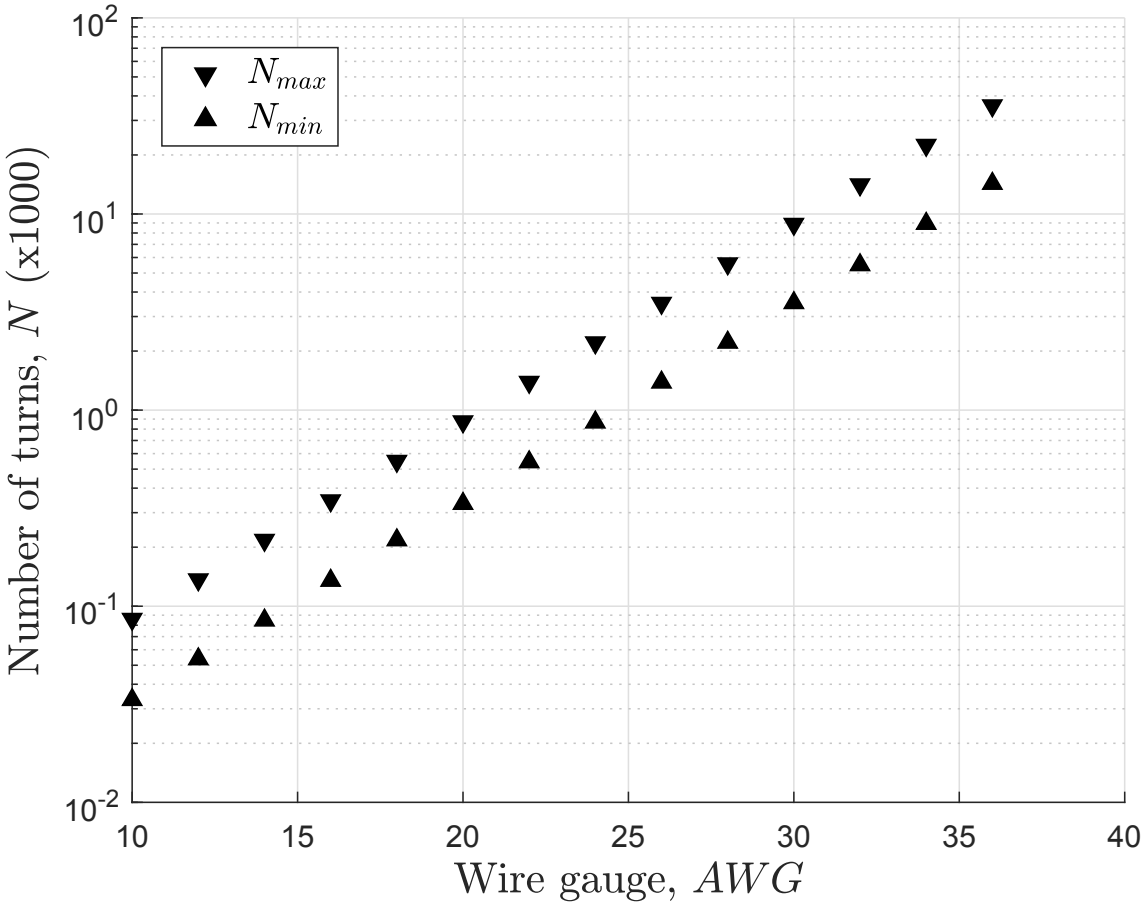

Figure 3.7: Maximum and minimum number of turns in function of wire gauge for the inner coil with $NI = 500\ A$

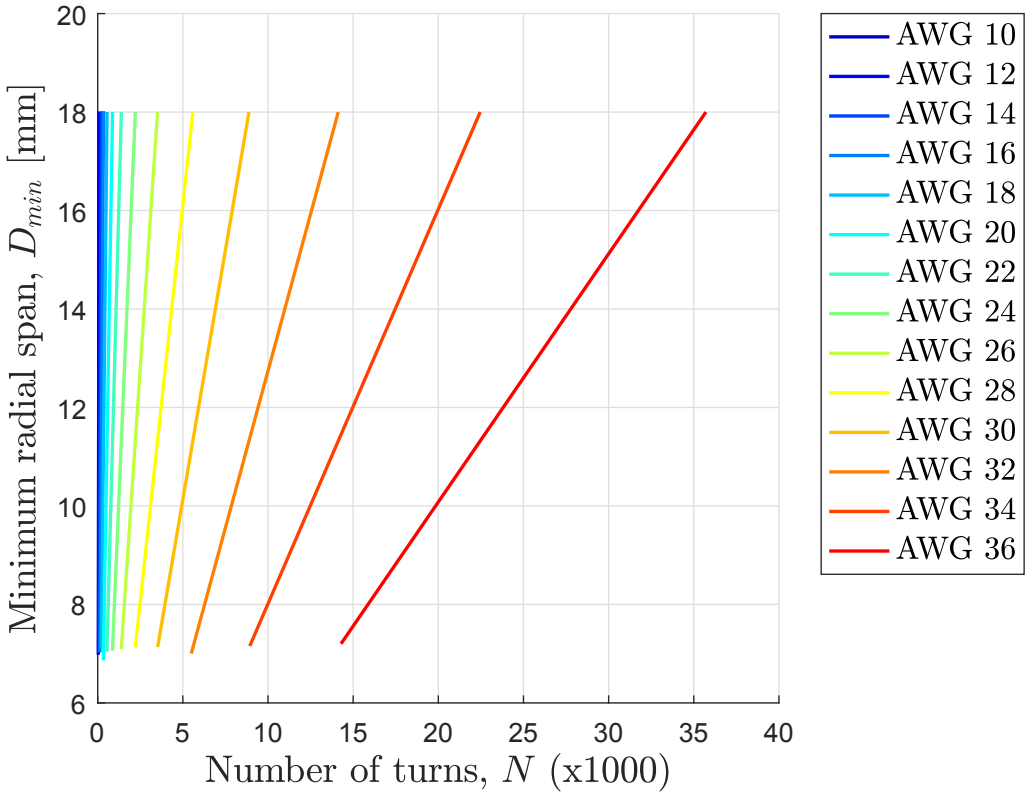

(a) Minimum radial span

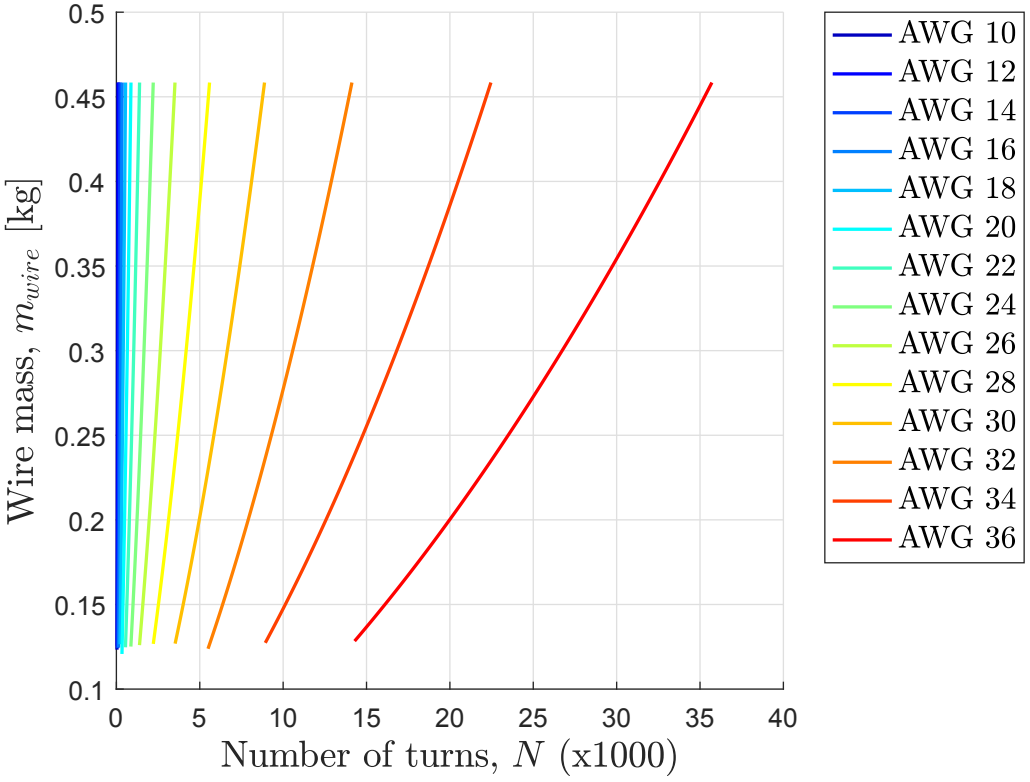

(b) Wire mass

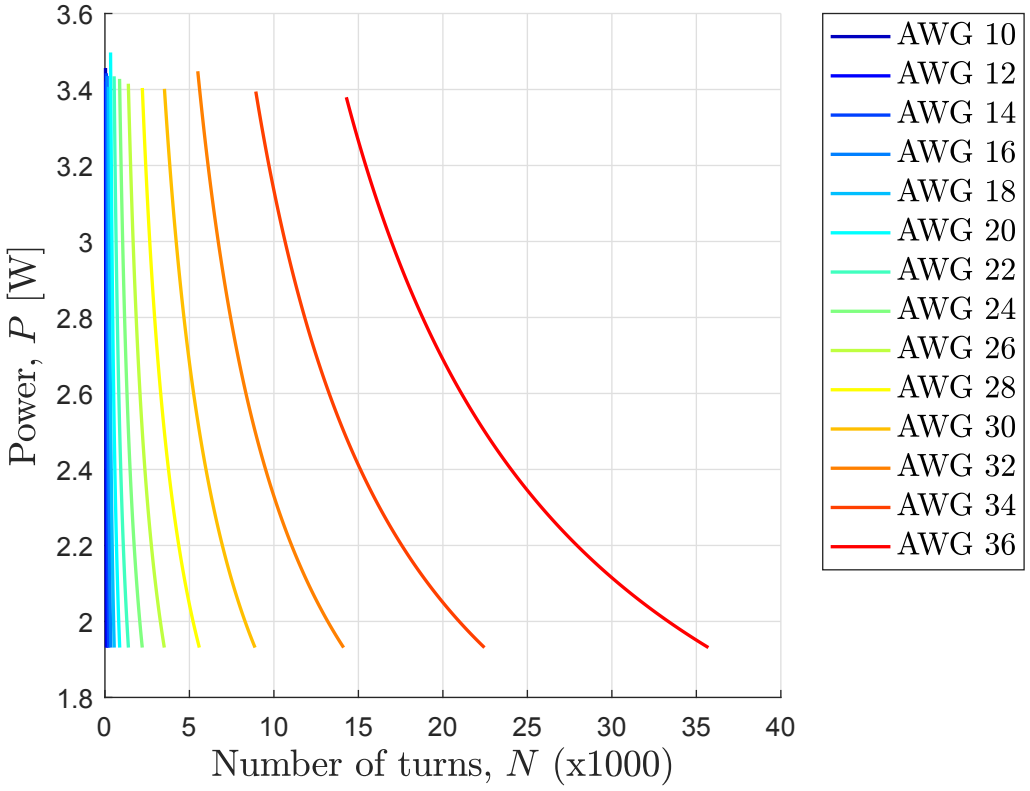

(c) Power input

Figure 3.8: Parametric study of the inner coil in modified pre-reference case with $NI = 500$

Repeating the analysis for the outer coils (and thence implementing any necessary modification to fulfil coil requirements) allows achieving a reference case for posterior simulations taking coil feasibility into account. It should be noted that finding an appropriate magnetic circuit with feasible-to-build coils is an iterative process. To accomplish this, it is generally necessary to follow a trial-and-error method, given that the parameters influencing the magnetic field — effective coil intensity and radial span — strongly influence the coil design study at the same time, rendering the problem coupled. It is possible to take advantage of the capabilities of the tool developed to launch batches of simulations modifying the mentioned parameters to attain a feasible case.

The resulting magnetic circuit, of which all parameters are shown by element in Table 3.3 [(1)(2)], produces the magnetic field displayed in Fig. 3.9. Furthermore, the power input to the circuit, as computed from post-processing (see Sec. 2.5.3),

[(1)] The reference frame is placed at the mean line of the discharge channel with $z = 0$ lying at the axially-outermost position, so that all elements are located at negative axial coordinates.

[(2)] Negative values in current intensity are used to indicate flow of electricity in the opposite direction.

is found to be

$$P_{mag} = 34.57\ W$$

consistently with the addition of all coil approximate input powers as returned by the analysis.

Element	**Parameter**	**Value**
Discharge channel	Axial span, Δz [mm]	25
	Radial span, Δr [mm]	15
	Minimum axial position, z_{min} [mm]	-25
	Minimum radial position, r_{min} [mm]	35
Inner coil	Axial span, Δz [mm]	40
	Radial span, Δr [mm]	15
	Minimum axial position, z_{min} [mm]	-48
	Minimum radial position, r_{min} [mm]	9
	Effective current intensity, NI [A]	500
	Number of turns, N	17500
	Current intensity, I [A]	0.0286
	Wire gauge (diameter), AWG (d [mm])	34 (0.16)
Inner-outer coil	Axial span, Δz [mm]	40
	Radial span, Δr [mm]	7
	Minimum axial position, z_{min} [mm]	-48
	Minimum radial position, r_{min} [mm]	65
	Effective current intensity, NI [A]	300
	Number of turns, N	6250
	Current intensity, I [A]	0.048
	Wire gauge (diameter), AWG (d [mm])	34 (0.16)
Outer-outer coil	Axial span, Δz [mm]	40
	Radial span, Δr [mm]	7
	Minimum axial position, z_{min} [mm]	-48
	Minimum radial position, r_{min} [mm]	78
	Effective current intensity, NI [A]	-500
	Number of turns, N	335
	Current intensity, I [A]	-1.4925
	Wire gauge (diameter), AWG (d [mm])	20 (0.81)

Inner front pole	Axial span, Δz [mm]	6
	Radial span, Δr [mm]	28
	Minimum axial position, z_{min} [mm]	-8
	Minimum radial position, r_{min} [mm]	0
	Material	Pure iron
Outer front pole	Axial span, Δz [mm]	6
	Radial span, Δr [mm]	28
	Minimum axial position, z_{min} [mm]	-8
	Minimum radial position, r_{min} [mm]	57
	Material	Pure iron
Back pole	Axial span, Δz [mm]	6
	Radial span, Δr [mm]	85
	Minimum axial position, z_{min} [mm]	-54
	Minimum radial position, r_{min} [mm]	0
	Material	Pure iron
Inner core	Axial span, Δz [mm]	40
	Radial span, Δr [mm]	9
	Minimum axial position, z_{min} [mm]	-48
	Minimum radial position, r_{min} [mm]	0
	Material	Pure iron
Outer core	Axial span, Δz [mm]	40
	Radial span, Δr [mm]	6
	Minimum axial position, z_{min} [mm]	-48
	Minimum radial position, r_{min} [mm]	72
	Material	Pure iron

Inner screen	Axial span, Δz [mm]	22
	Radial span, Δr [mm]	1
	Minimum axial position, z_{min} [mm]	-48
	Minimum radial position, r_{min} [mm]	29
	Material	Pure iron
Outer screen	Axial span, Δz [mm]	20
	Radial span, Δr [mm]	1
	Minimum axial position, z_{min} [mm]	-48
	Minimum radial position, r_{min} [mm]	60
	Material	Pure iron

Table 3.3: Magnetic elements and parameters in reference case

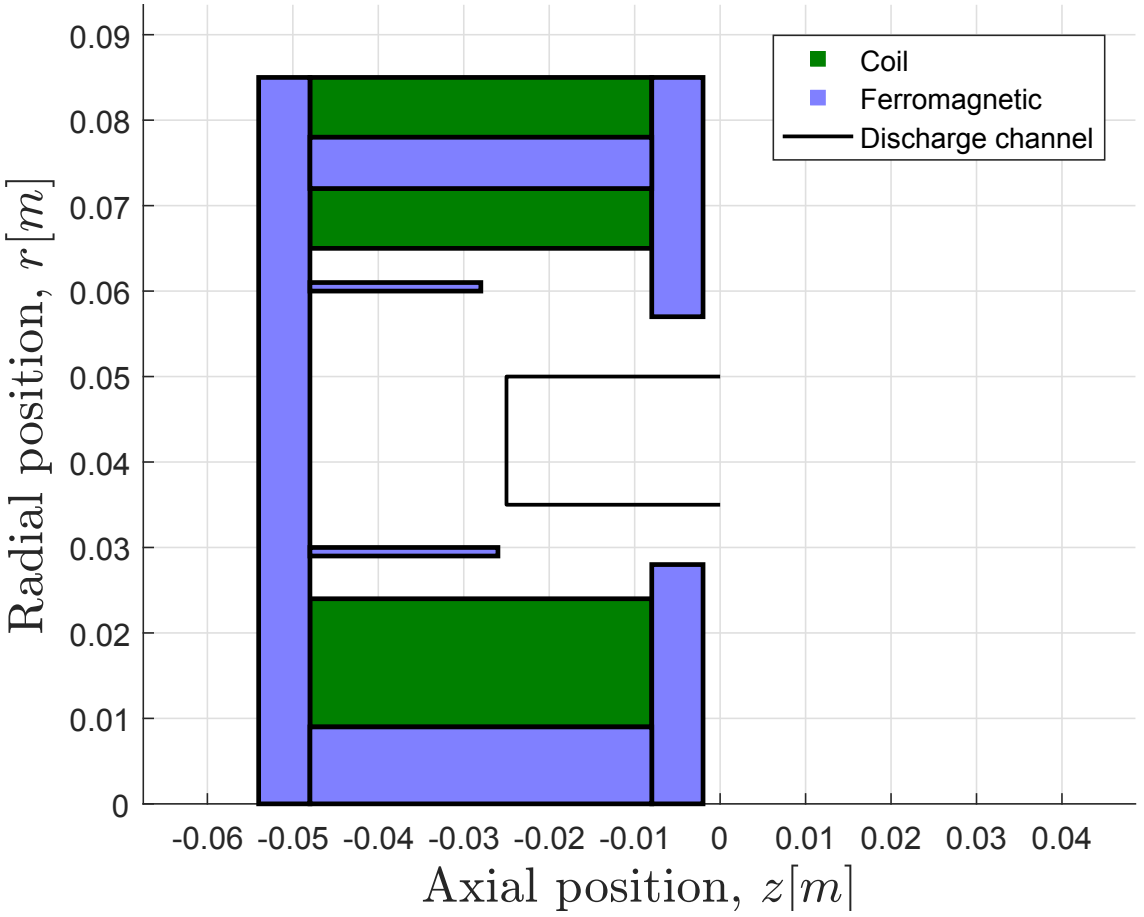

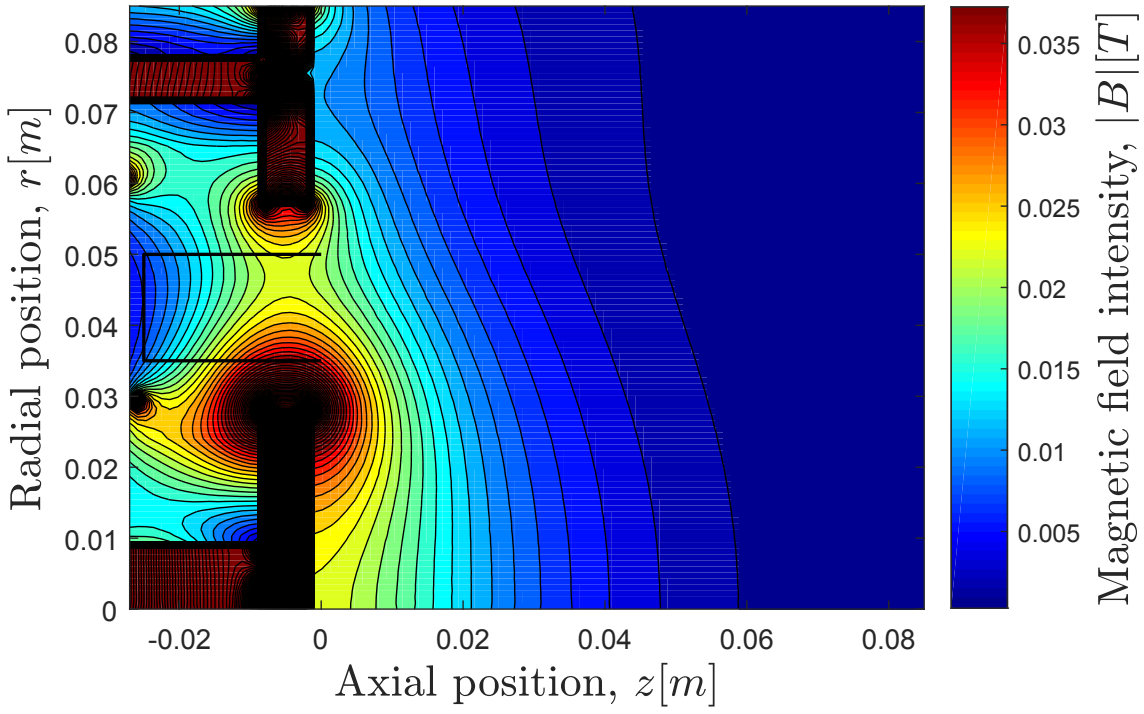

(b) Magnetic field intensity

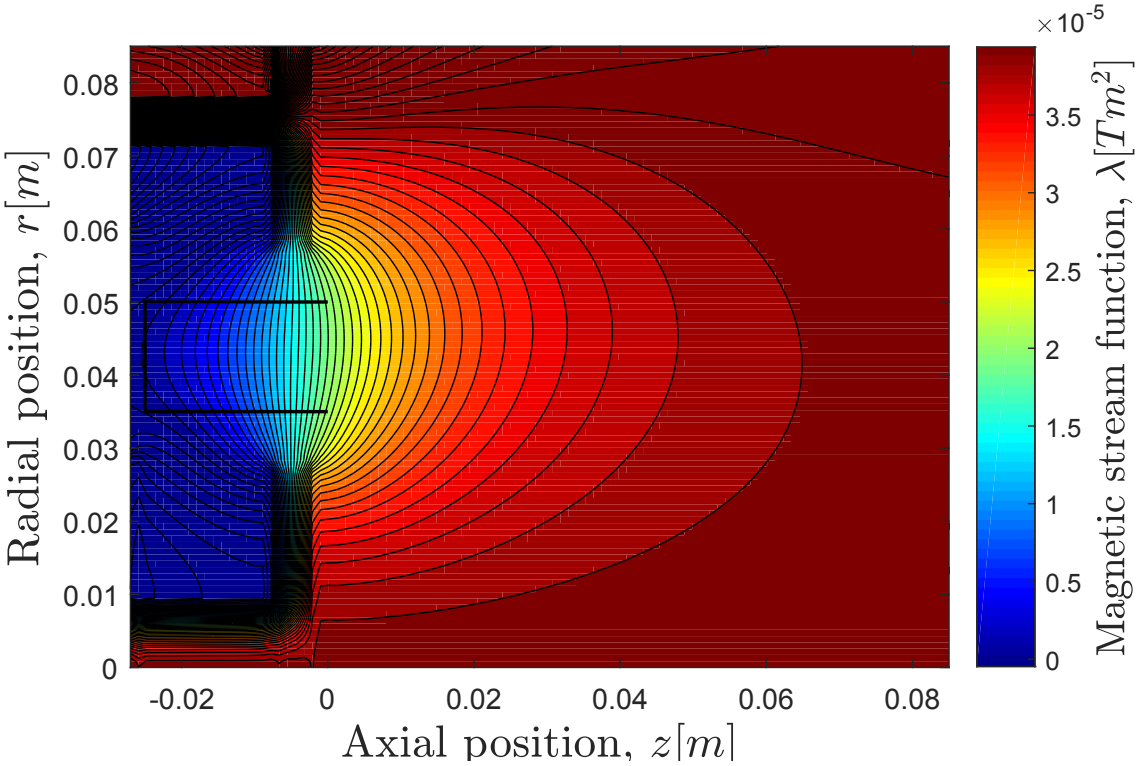

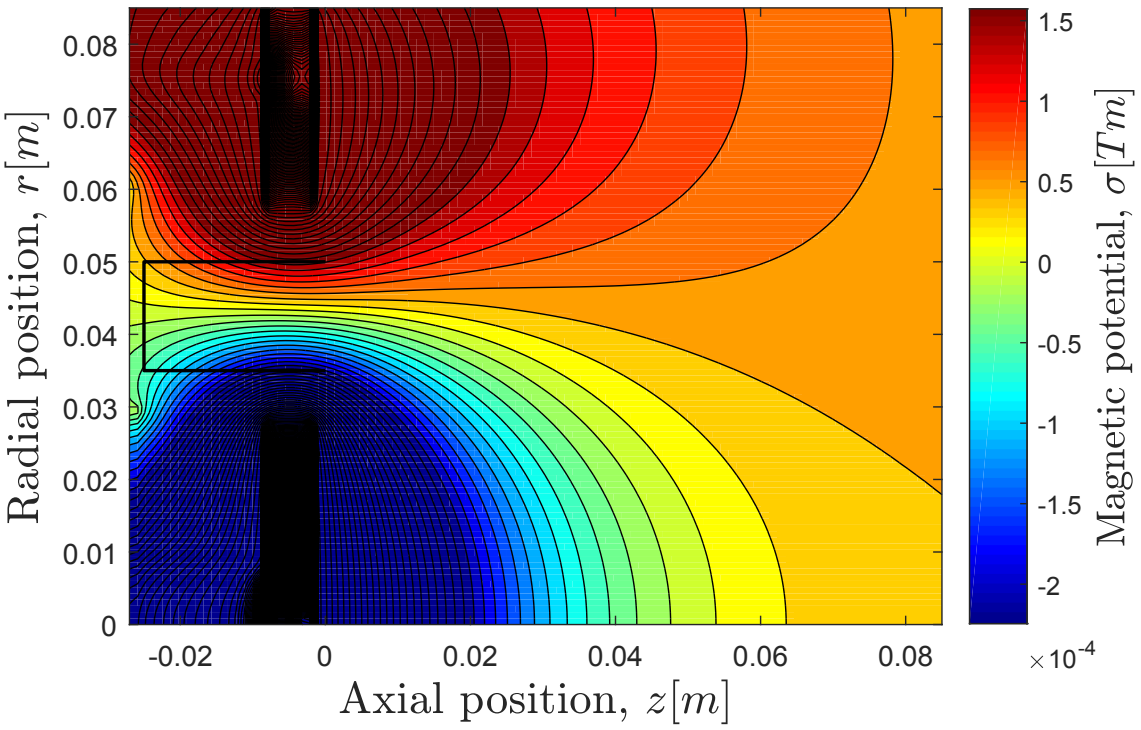

(d) Magnetic potential

Figure 3.9: Reference case (definitive)

On the basis of a definitive reference case with coils designed to be feasible to be manufactured and used under the required operating conditions, it is possible to start the pursuit of achieving particular magnetic topographies and to run batches of simulations.

3.5 Singular-point topography

A magnetic field presenting a singularity ($|B| = 0$) at a point within the discharge channel is an expected configuration in different types of thrusters.

Certain designs include the singular point on purpose, claiming that it helps towards the improvement of the current intensity of the thruster, but this effect is yet to be explored. In addition, it has been found that this configuration tends to reduce wall erosion and low-frequency current oscillations, therefore attaining a better performance [20]. On the other hand, in a number of cases, it may simply appear consequent to the magnetic circuit implemented. For instance, helicon or ECR thrusters, in which there is no anode, commonly present a singularity at the rear, given that a permanent magnet is used to magnetically shield the end of the channel.

On account of the aforementioned, it is a necessary asset to have the capability of simulating this topography, as the author's code may be used along with the HYPHEN platform. Producing such magnetic field is relevant both regarding the attainment of the corresponding magnetic circuit and the ability to simulate the physics of the plasma under this field.

Hereunder, two different strategies to achieve the singular-point topography will be put forward.

3.5.1 Open circuit approach

In the first place, it is possible to attain a singularity mainly by means of the deletion of the back pole, thus implying a non-closed ferromagnetic casing.

The mentioned feature is advantageous from the perspective of weight saving. Nonetheless, with the aim of producing a similar magnetic field intensity at the discharge, it clearly imposes the need of higher effective coil current intensities as the ferromagnetic part is open, therefore requiring a larger power input. Furthermore, the resulting circuit geometry may result impractical.

To generate the topography, a new magnetic circuit is built on the basis of the reference case (Fig. 3.9). From all the elements in the new circuit, the parameters that differ from the reference case (Table 3.3) are collected in Table 3.4[3][4].

[3] The reference frame is placed at the mean line of the discharge channel with $z = 0$ lying at the axially-outermost position, so that all elements are located at negative axial coordinates.

[4] Negative values in current intensity are used to indicate flow of electricity in the opposite direction.

Element	**Parameter**	**Value**
Inner coil	Axial span, Δz [mm]	50
	Radial span, Δr [mm]	20
	Minimum axial position, z_{min} [mm]	-53
	Effective current intensity, NI [A]	1800
	Number of turns, N	1200
	Current intensity, I [A]	1.5
	Wire gauge (diameter), AWG (d [mm])	20 (0.81)
Inner-outer coil	Axial span, Δz [mm]	50
	Radial span, Δr [mm]	10
	Minimum axial position, z_{min} [mm]	-53
	Minimum radial position, r_{min} [mm]	59
	Effective current intensity, NI [A]	750
	Number of turns, N	15000
	Current intensity, I [A]	0.0467
Outer-outer coil	Axial span, Δz [mm]	50
	Radial span, Δr [mm]	10
	Minimum axial position, z_{min} [mm]	-53
	Minimum radial position, r_{min} [mm]	75
	Effective current intensity, NI [A]	-700
	Number of turns, N	14750
	Current intensity, I [A]	-0.0475
	Wire gauge (diameter), AWG (d [mm])	34 (0.16)
Inner front pole	Axial span, Δz [mm]	3
	Radial span, Δr [mm]	31
	Minimum axial position, z_{min} [mm]	-3

Outer front pole	Axial span, Δz [mm]	3
	Radial span, Δr [mm]	31
	Minimum axial position, z_{min} [mm]	-3
	Minimum radial position, r_{min} [mm]	54
Inner core	Axial span, Δz [mm]	50
	Minimum axial position, z_{min} [mm]	-53
Outer core	Axial span, Δz [mm]	50
	Minimum axial position, z_{min} [mm]	-53
	Minimum radial position, r_{min} [mm]	69

Table 3.4: Magnetic elements and parameters different from the reference case in singular-point topography (open circuit approach)

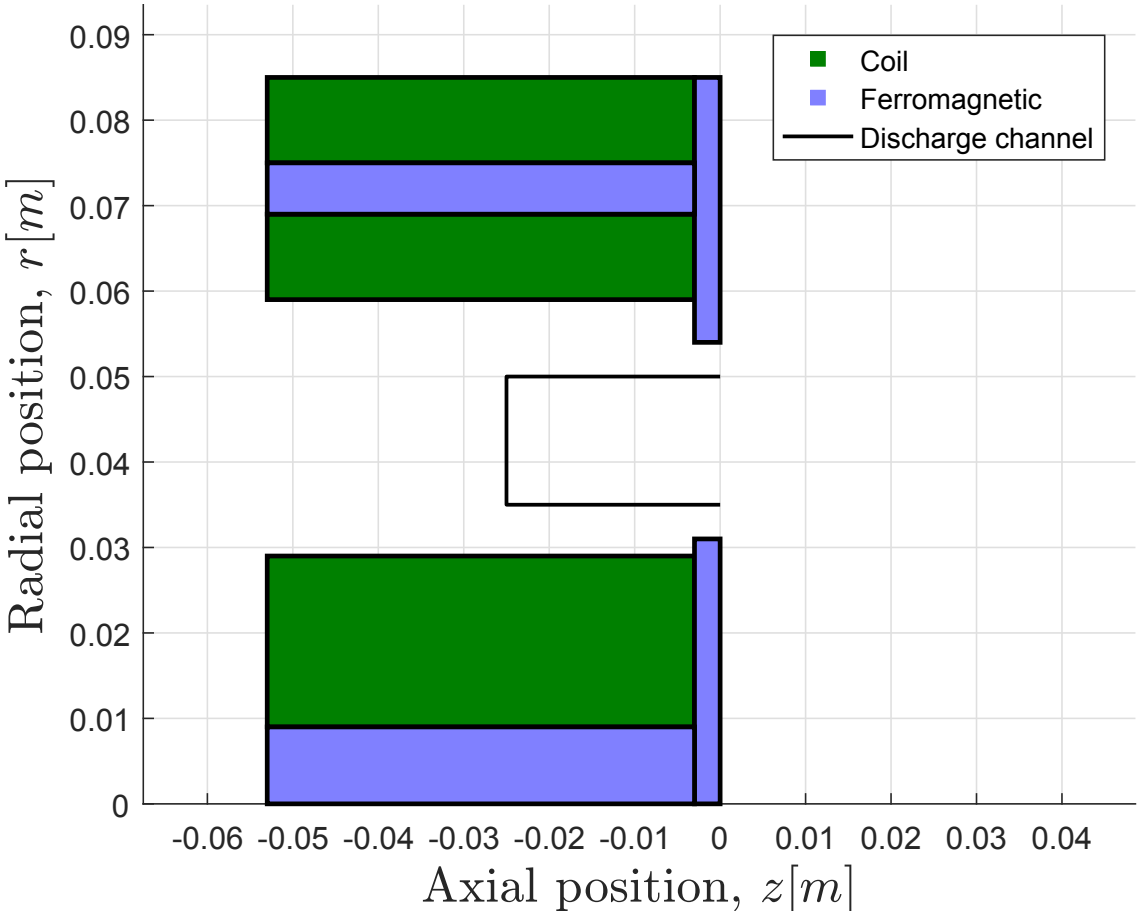

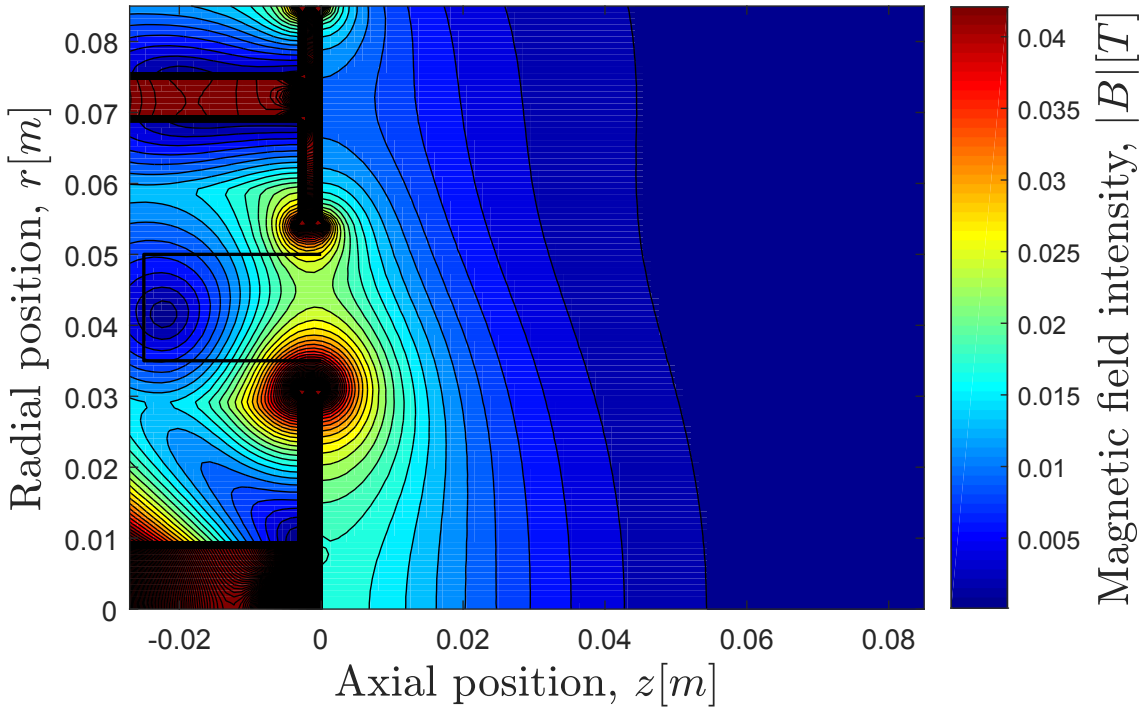

(b) Magnetic field intensity

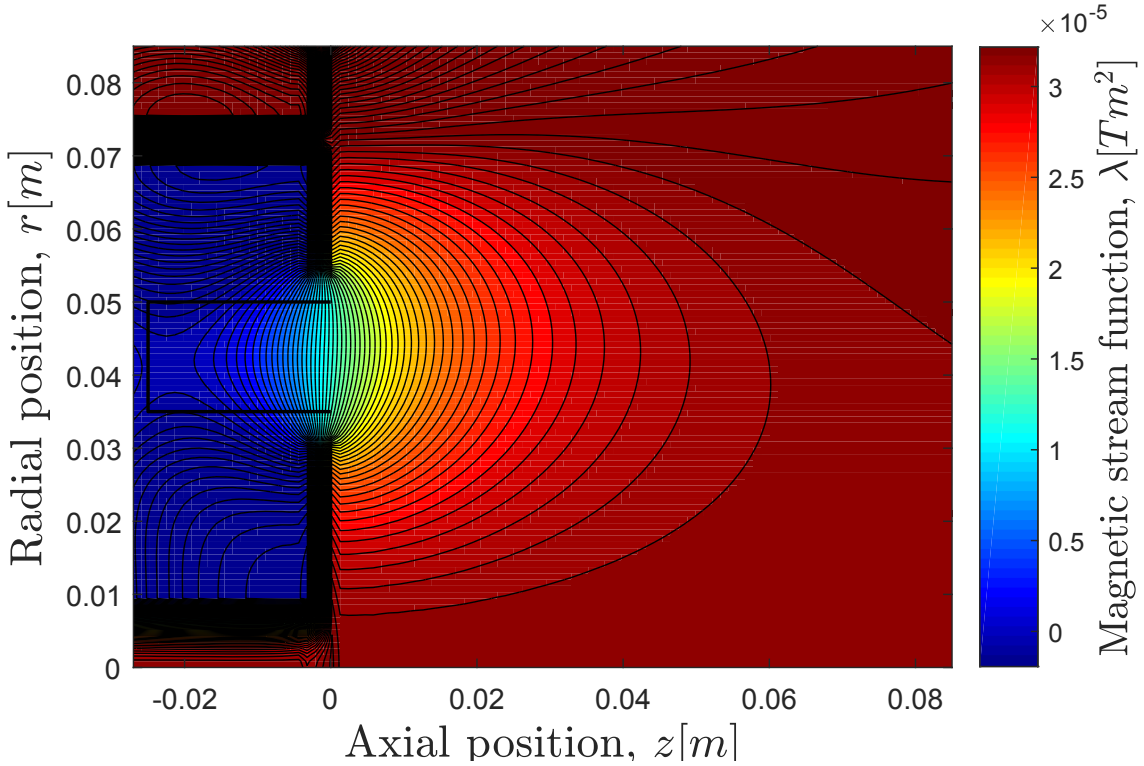

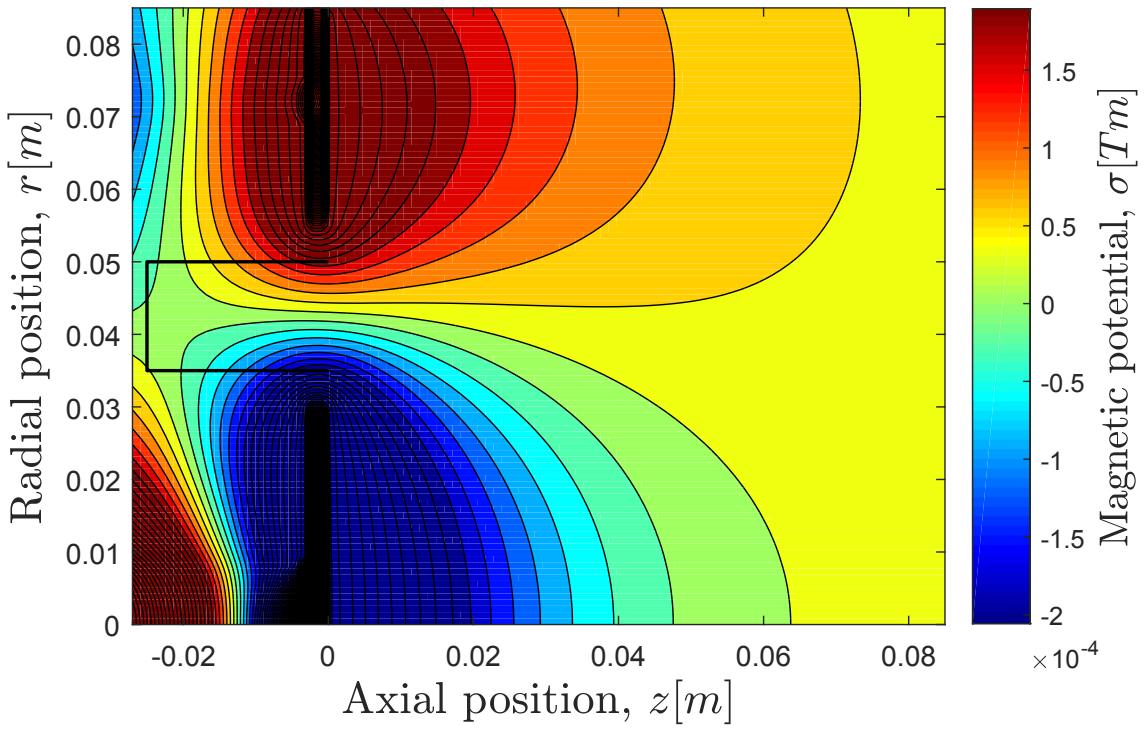

(d) Magnetic potential

Figure 3.10: Singular point-topography (open circuit approach)

In accordance with the aforementioned, no ferromagnetic back pole is included (note that, for the purpose of manufacturability, a non-ferromagnetic back pole may be used). In addition, it is necessary to exclude the magnetic screens from the circuit. Note that the length of the thruster and the radial span of the active elements are increased with respect to the reference case to fulfil coil design requirements (feasibility).

As aforementioned, the power input to the circuit is notably higher. Computed from post-processing (see Sec. 2.5.3), it is found to be

$$P_{mag} = 67.95\ W$$

approximately twice as that required by the reference circuit, for a similar field intensity.

3.5.2 Trim magnet approach

It is further possible to attain the singular-point topography by means of the addition of a permanent magnet at the rear part, as it is typically done in ECR and helicon thrusters (or using a trim coil with the same effect) [21], between the anode and the back pole in the case of a Hall one. The magnetic field generated by the magnet is able to cancel out the contributions of the active elements, producing a singularity in the discharge channel.

Including a neodymium-iron-boron magnet in the reference circuit, with the properties detailed in Table 3.5[(5)], results in the topography observed in Fig. 3.11. Note that it is necessary to increase slightly the effective current intensity of the inner-outer coil to maintain radial symmetry with respect to the mean line of the channel. The corresponding power input to the circuit is roughly that of the reference case ($P_{mag} = 34.54\ W$).

[(5)] The reference frame is placed at the mean line of the discharge channel with $z = 0$ lying at the axially-outermost position, so that all elements are located at negative axial coordinates.

Element	**Parameter**	**Value**
Inner-outer coil	Effective current intensity, NI [A]	325
	Number of turns, N	7500
	Current intensity, I [A]	0.0433
Trim magnet	Axial span, Δz [mm]	40
	Radial span, Δr [mm]	15
	Minimum axial position, z_{min} [mm]	-42
	Minimum radial position, r_{min} [mm]	35
	Magnet type	NdFeB 32 MGOe

Table 3.5: Magnetic elements and parameters different from the reference case in singular-point topography (trim magnet approach)

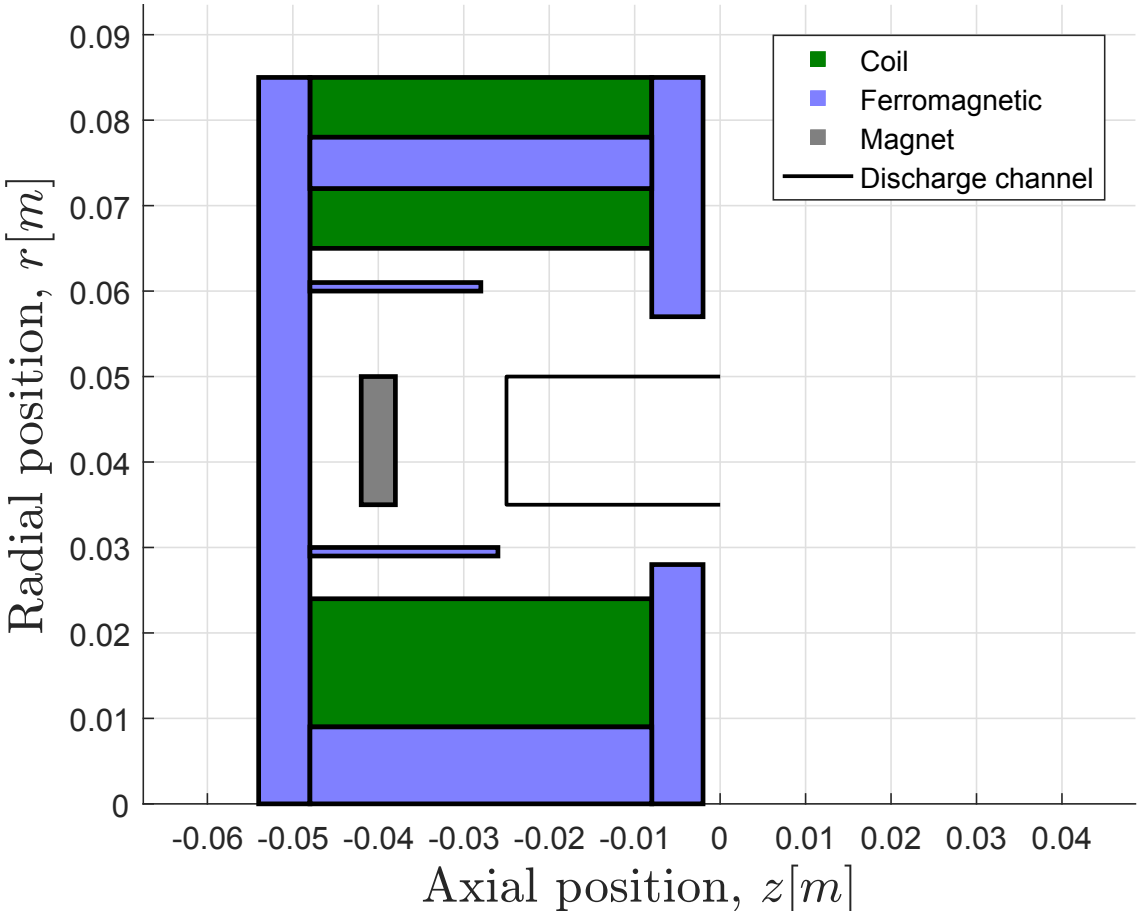

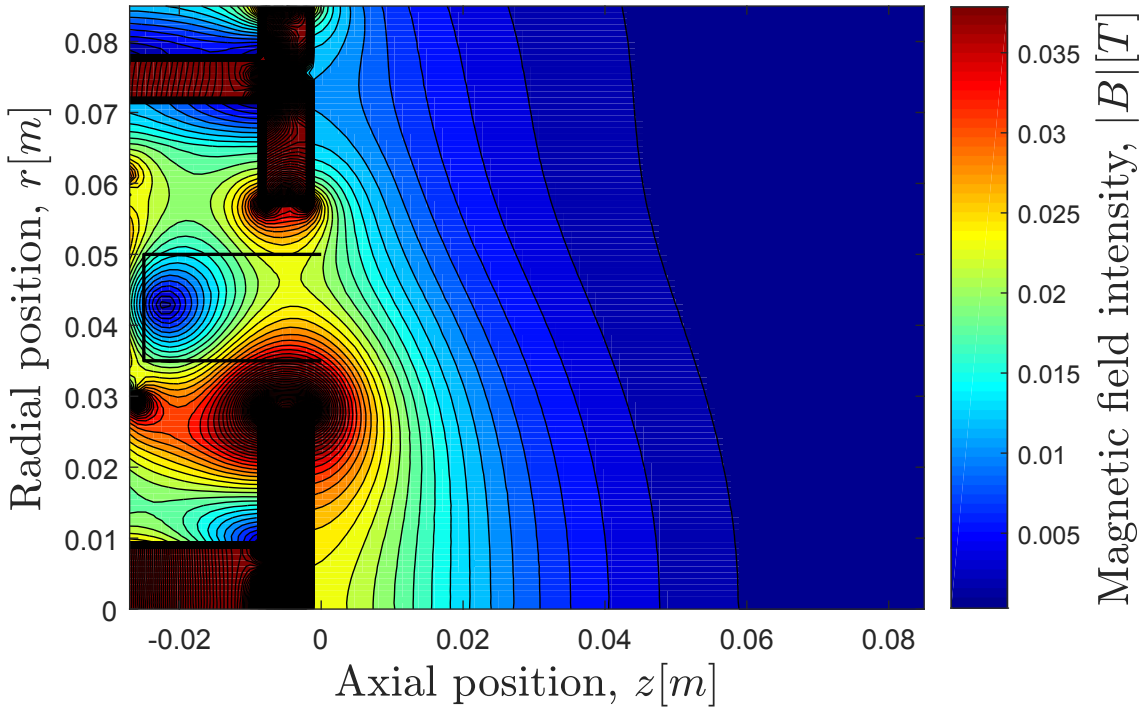

(b) Magnetic field intensity

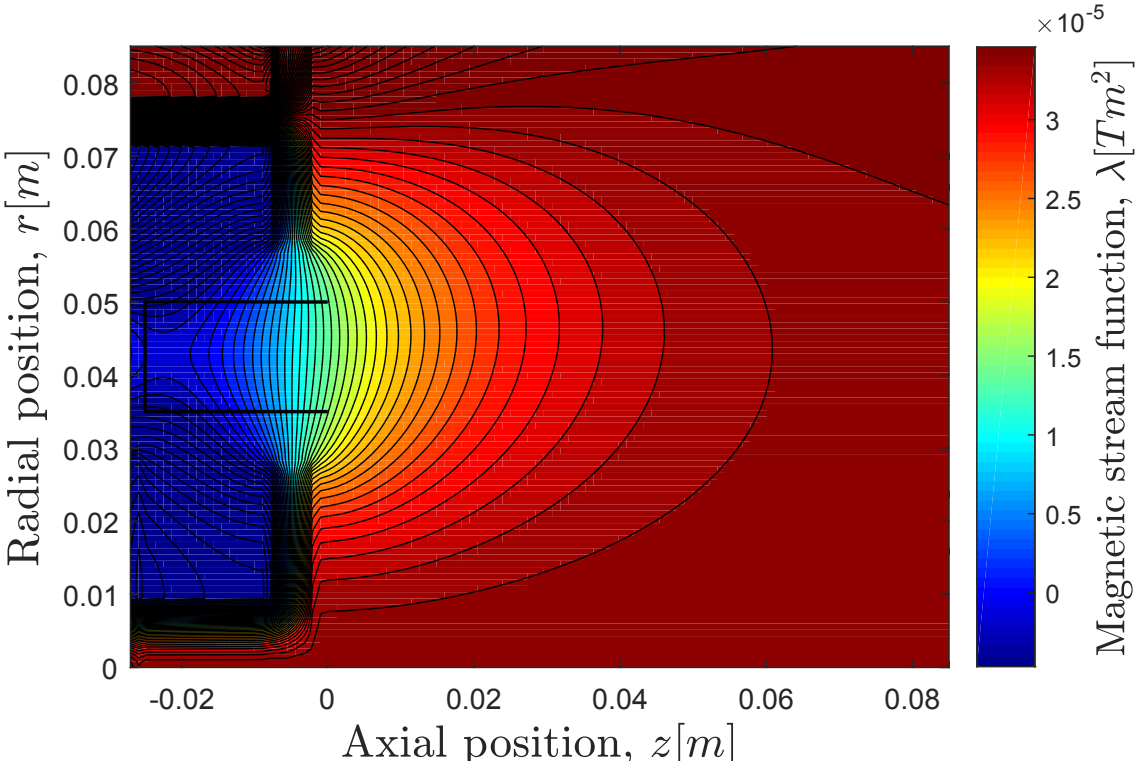

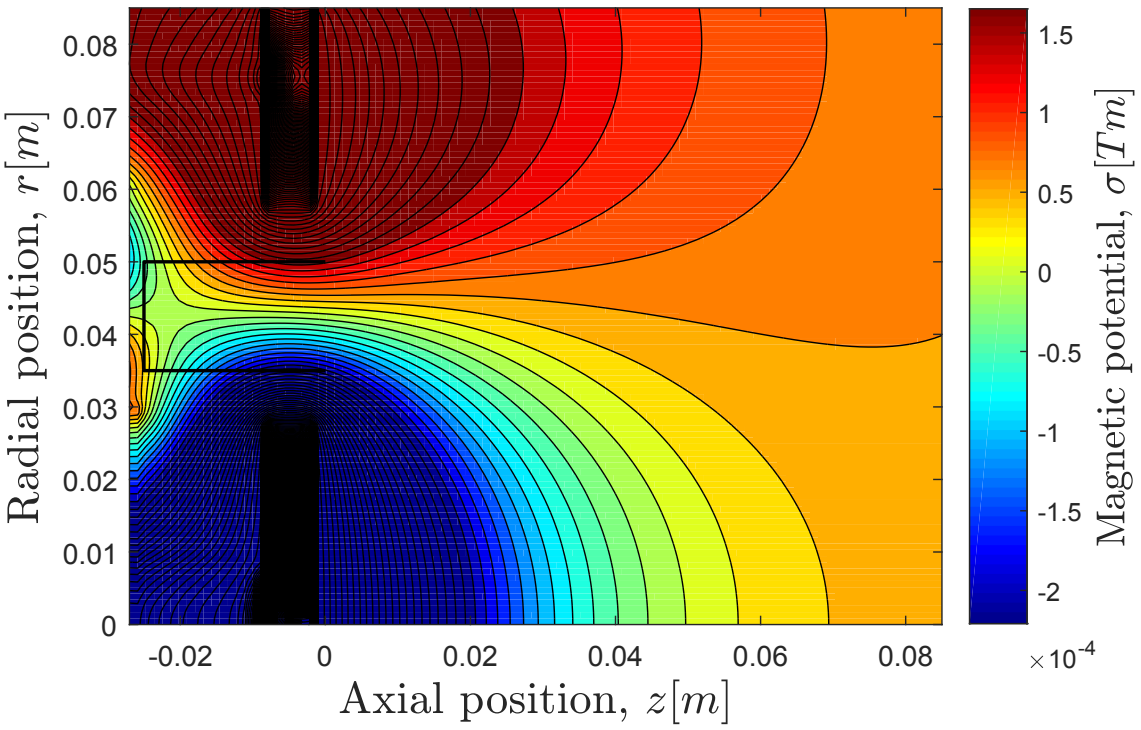

(d) Magnetic potential

Figure 3.11: Singular point-topography (trim magnet approach)

3.6 Magnetic shielding

3.6.1 Definition and justification

Within ERS, the concept of magnetic shielding (MS) consists in the implementation of a magnetic topography which aims at protecting the ceramic walls of the discharge channel from erosion.

The magnetic streamlines inside the channel in this configuration are strongly concave in the axial direction, ideally parallel to the walls. Theoretically, the potential at them is close to the anode potential and electron temperature along the lines is therefore relatively small [16]. Ultimately, the plasma-wall interaction is reduced.

Mikellides et al. conclude a decrease of ion flux to the walls in around one order of magnitude with respect to a non-shielded configuration [22]. Nonetheless, on the basis of theoretical ion bombardment erosion models, it is found that the main mechanism responsible for erosion reduction in MS may not be the magnetic topography itself but the downstream shift of the acceleration region [17], which is consequent to the MS configuration.

On the other hand, the lines close to the exit of the channel are concave in MS. This is known as plasma lensing, and is supposed to improve efficiency by decreasing plume divergence. As a matter of fact, Pérez Grande et al. assert that this feature must be present in the topography of the thruster to avoid a trade-off between performance degradation and erosion reduction [17].

Examples of thrusters taking advantage of the MS configuration are H6MS, NASA 300-MS, MaSMi and NASA-173Mv1. The magnetic topography of the latter is shown in Fig. 3.12 as an illustration.

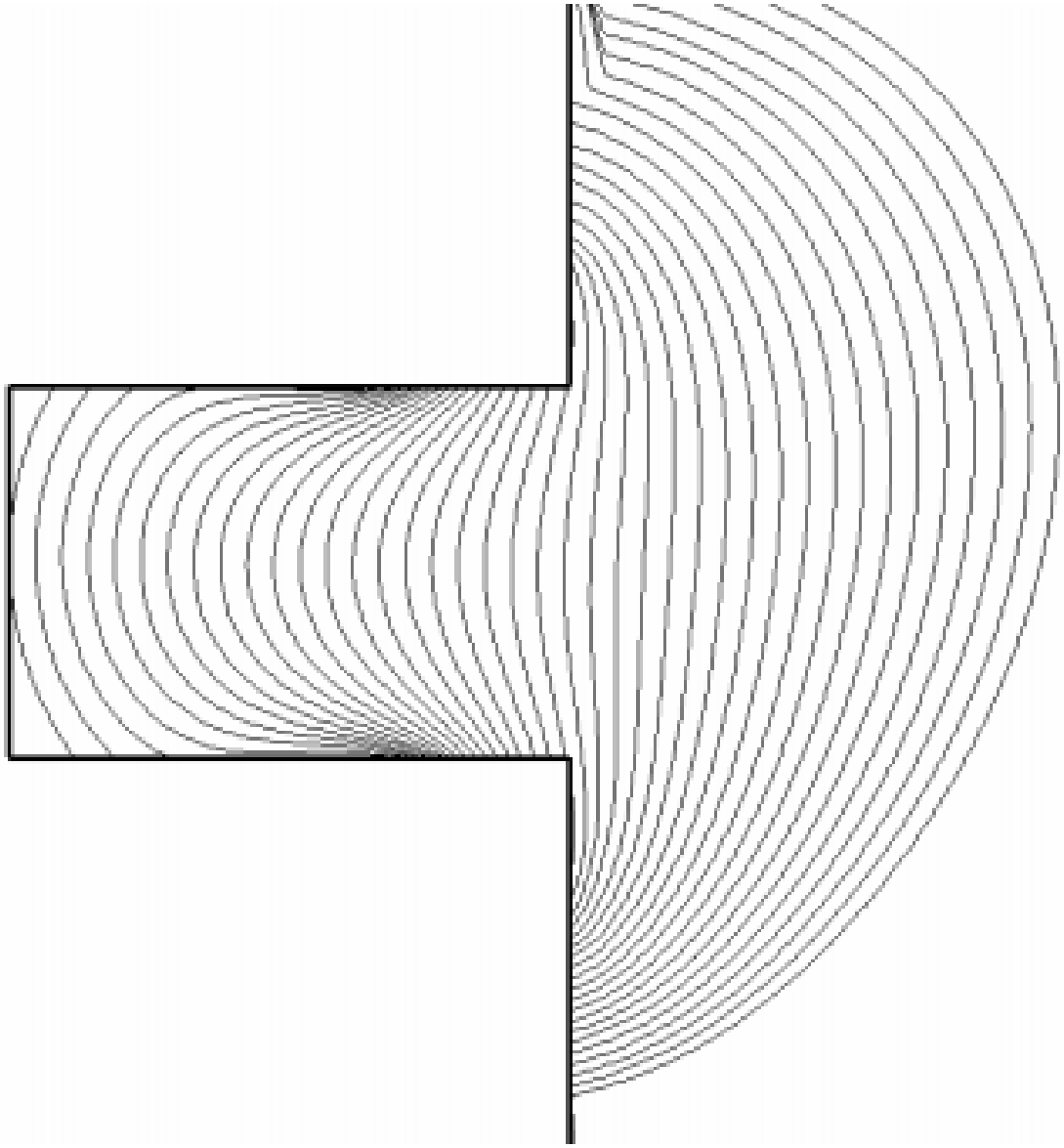

Figure 3.12: Magnetic field topography of the NASA-173Mv1. *Source: [2]*

3.6.2 Topography attained

Backed up by several simulations of different magnetic circuits, it is found that magnetic screens play an essential role towards the achievement of MS. The magnetic topography inside the discharge channel is very sensitive to changes in screen parameters. These elements are able to "push" the magnetic lines to curve them into the concave shape sought.

To demonstrate the capabilities of the author's tool and to show the evolution of the magnetic circuit towards MS, a simultaneous batch of intermediate geometries between the reference case and the MS topography is performed (see Fig. 3.13).

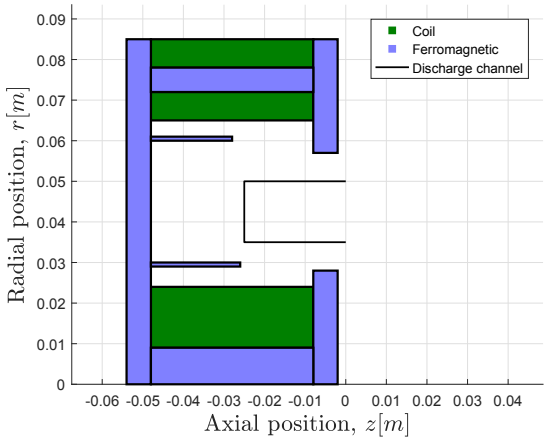

(a) Geometry

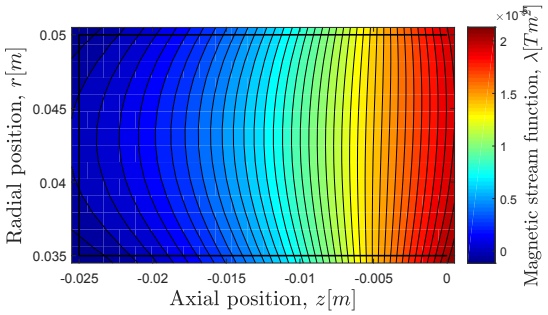

(b) Magnetic stream function

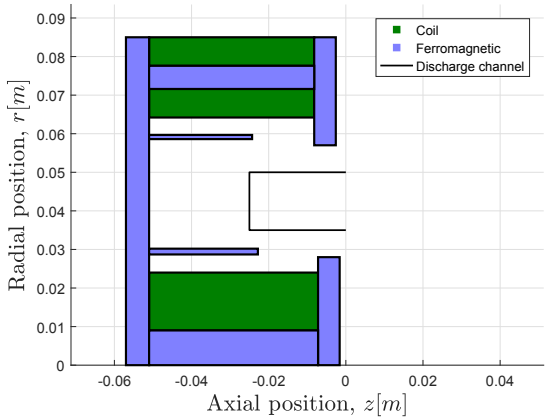

(c) Geometry

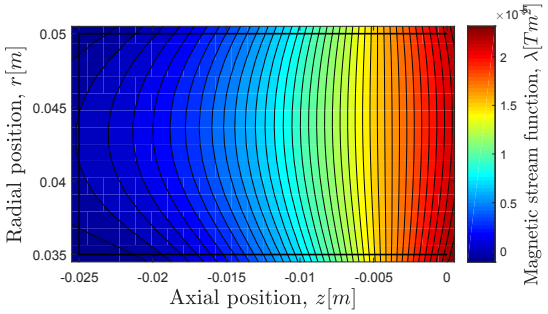

(d) Magnetic stream function

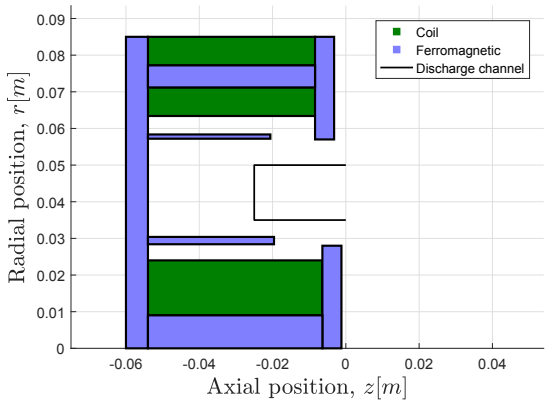

(e) Geometry

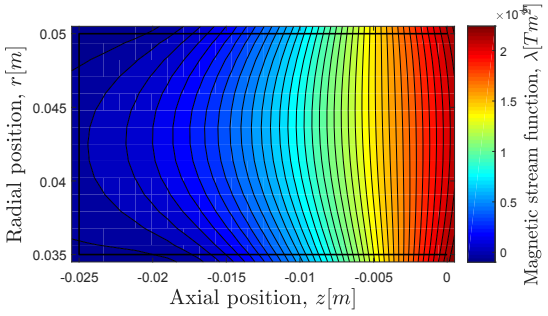

(f) Magnetic stream function

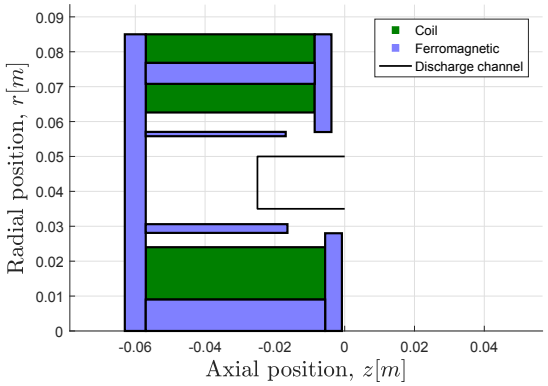

(g) Geometry

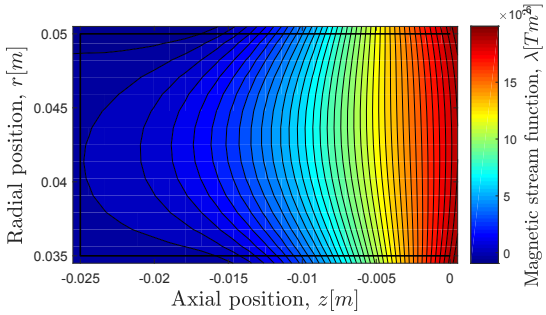

(h) Magnetic stream function

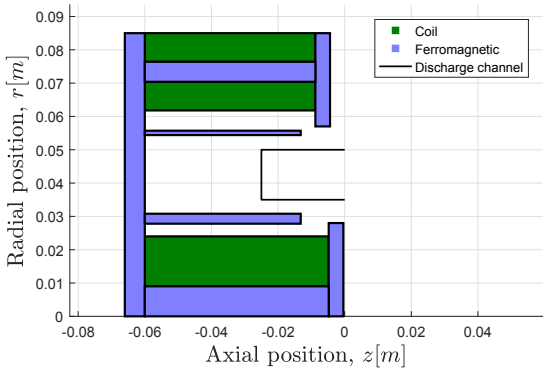

(i) Geometry

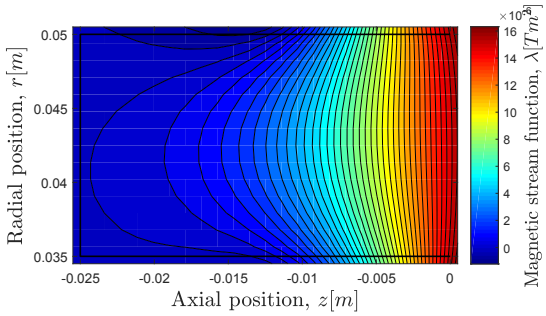

(j) Magnetic stream function

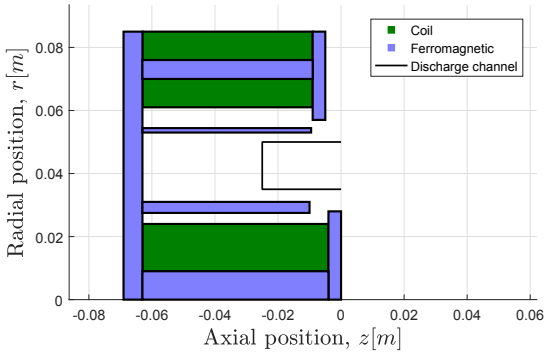

(k) Geometry

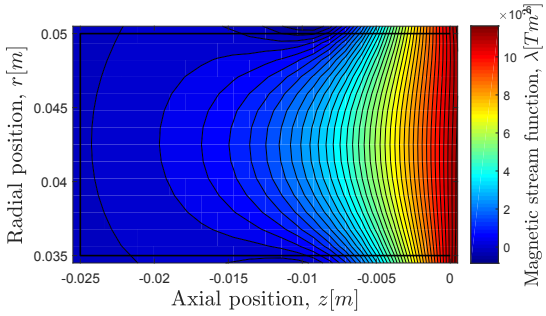

(l) Magnetic stream function

Figure 3.13: Evolution of the magnetic circuit from the reference case to the MS topography: geometry (left) and magnetic streamlines in the discharge channel (right)

Complete magnetic characteristics of the MS topography attained are shown in Fig. 3.14 and Fig. 3.15, of which all elements and parameters modified with respect to the reference case are displayed in Table 3.6[(6)(7)]. Note that, to maintain the maximum field intensity in the channel, the required power input is necessarily larger than in the reference case. Computed through the simulation it is $P_{mag} = 58.46\ W$.

With regard to shaping the magnetic lines to attain a MS topography, the fundamental step, as aforementioned, is the rise in screen dimensions. The axial extension of these elements causes the streamlines to bend as desired. On the other hand, changes in radial span are required to maintain the radial symmetry with respect to the mean line of the channel; the inner screen needs to be thicker since it is radially inward, thence possessing a smaller ferromagnetic volume in 3D than the outer one.

Modifications of parameters of active elements in Table 3.6 are simply introduced to fulfil coil feasibility requirements.

All remaining changes, in addition to radial span differences in screens, are responsible for keeping the channel mean-line radial symmetry.

[(6)] The reference frame is placed at the mean line of the discharge channel with $z = 0$ lying at the axially-outermost position, so that all elements are located at negative axial coordinates.

[(7)] Negative values in current intensity are used to indicate flow of electricity in the opposite direction.

Element	**Parameter**	**Value**
Inner coil	Axial span, Δz [mm]	59
	Minimum axial position, z_{min} [mm]	-63
	Effective current intensity, NI [A]	1250
	Number of turns, N	41000
	Current intensity, I [A]	0.0305
	Wire gauge (diameter), AWG (d [mm])	36 (0.13)
Inner-outer coil	Axial span, Δz [mm]	54
	Radial span, Δr [mm]	9
	Minimum axial position, z_{min} [mm]	-63
	Minimum radial position, r_{min} [mm]	61
	Effective current intensity, NI [A]	475
	Number of turns, N	21400
	Current intensity, I [A]	0.0222
	Wire gauge (diameter), AWG (d [mm])	36 (0.13)
Outer-outer coil	Axial span, Δz [mm]	54
	Radial span, Δr [mm]	9
	Minimum axial position, z_{min} [mm]	-63
	Minimum radial position, r_{min} [mm]	76
	Effective current intensity, NI [A]	-850
	Number of turns, N	570
	Current intensity, I [A]	-1.4912
Inner front pole	Axial span, Δz [mm]	4
	Minimum axial position, z_{min} [mm]	-4
Outer front pole	Axial span, Δz [mm]	4
	Minimum axial position, z_{min} [mm]	-9

Back pole	Minimum axial position, z_{min} [mm]	-69
Inner core	Axial span, Δz [mm]	59
	Minimum axial position, z_{min} [mm]	-63
Outer core	Axial span, Δz [mm]	54
	Minimum axial position, z_{min} [mm]	-63
	Minimum radial position, r_{min} [mm]	70
Inner screen	Axial span, Δz [mm]	53
	Radial span, Δr [mm]	3.5
	Minimum axial position, z_{min} [mm]	-63
	Minimum radial position, r_{min} [mm]	27.5
Outer screen	Axial span, Δz [mm]	53.5
	Radial span, Δr [mm]	1.4
	Minimum axial position, z_{min} [mm]	-63
	Minimum radial position, r_{min} [mm]	53

Table 3.6: Magnetic elements and parameters different from the reference case in magnetic shielding topography

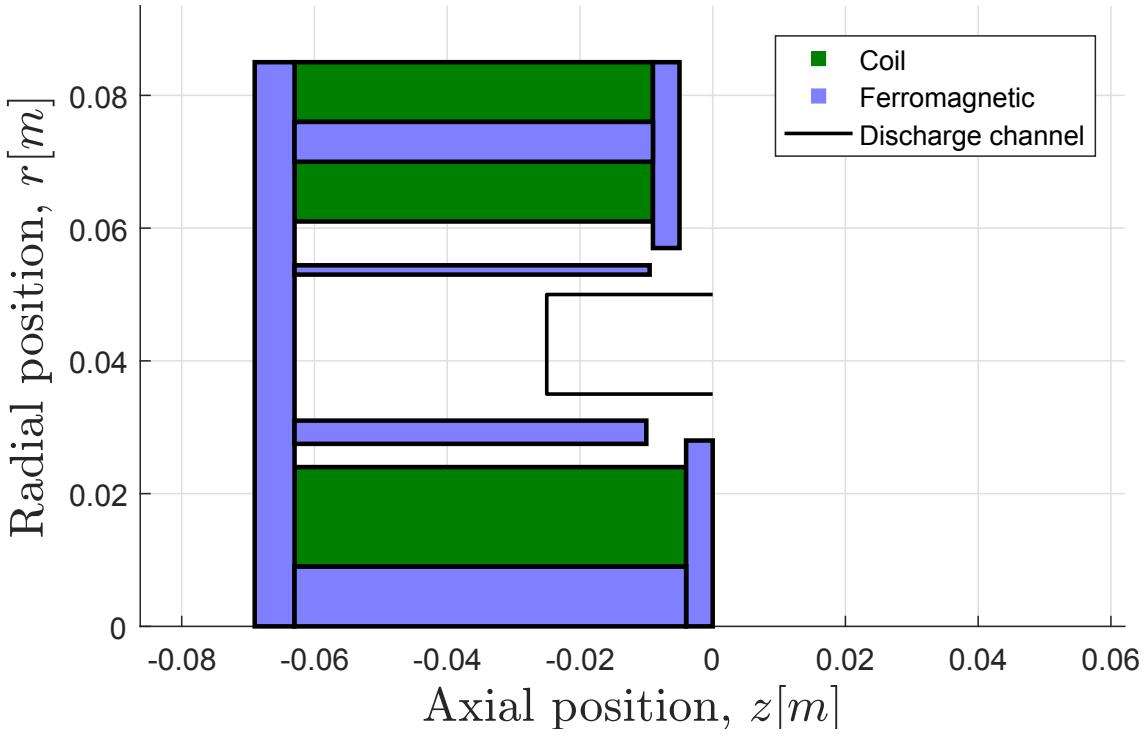

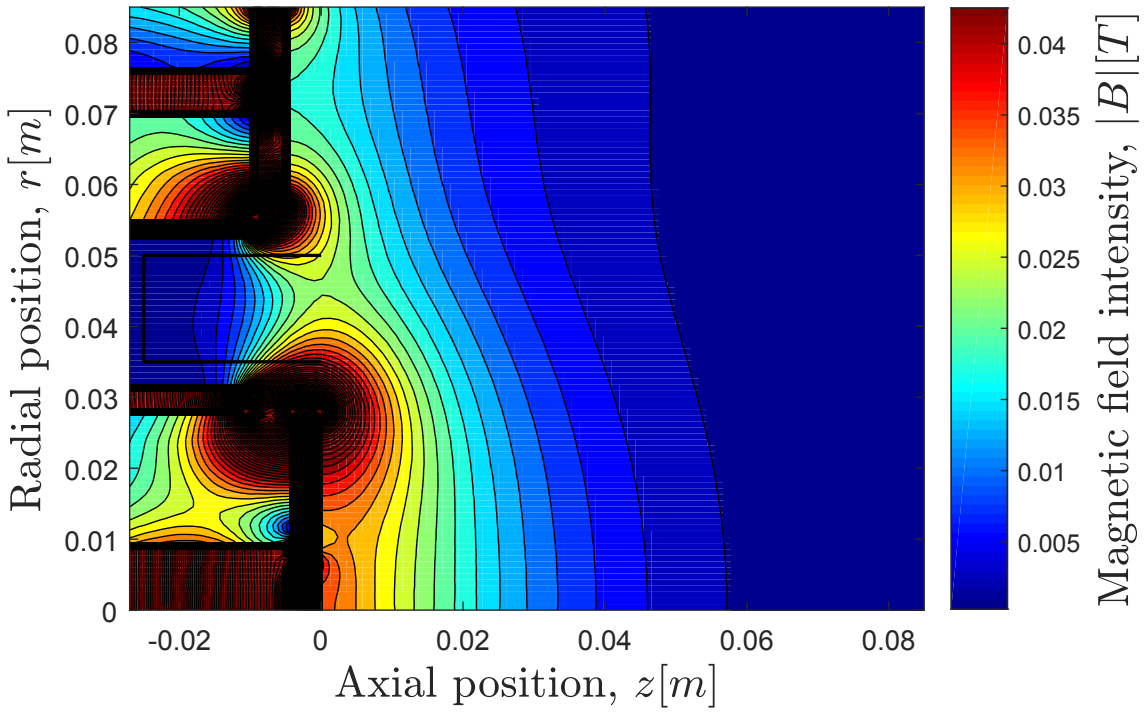

(b) Magnetic field intensity

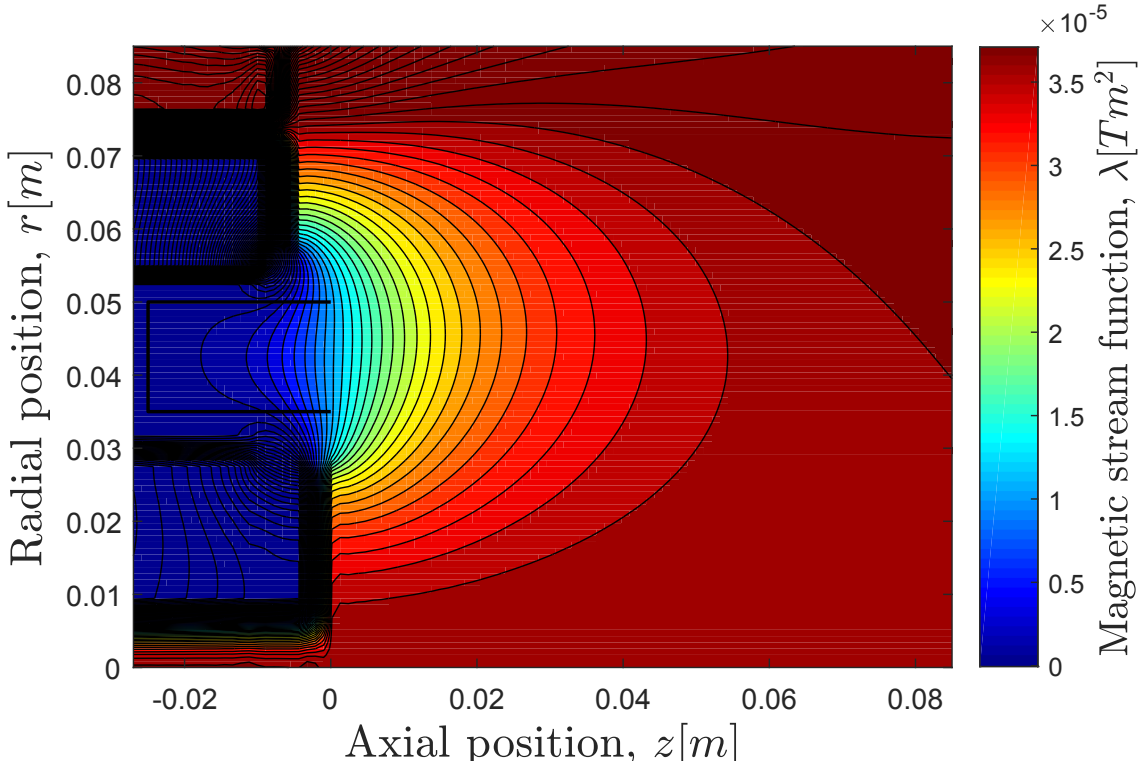

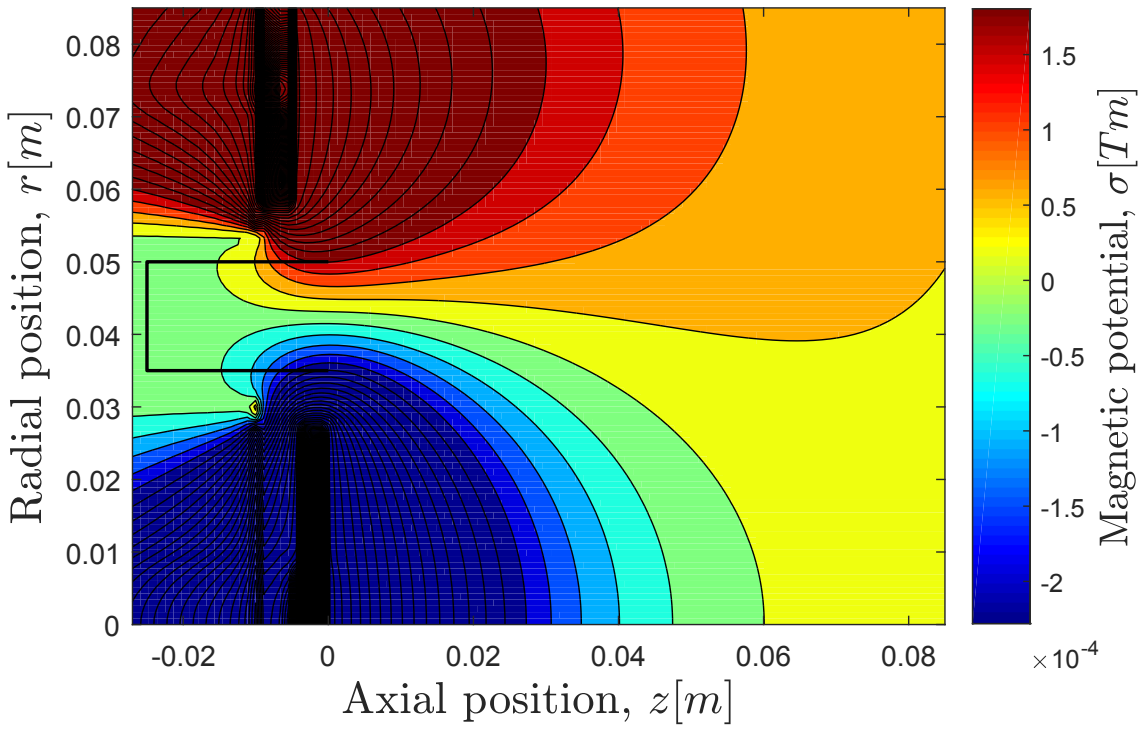

(d) Magnetic potential

Figure 3.14: Magnetic shielding topography

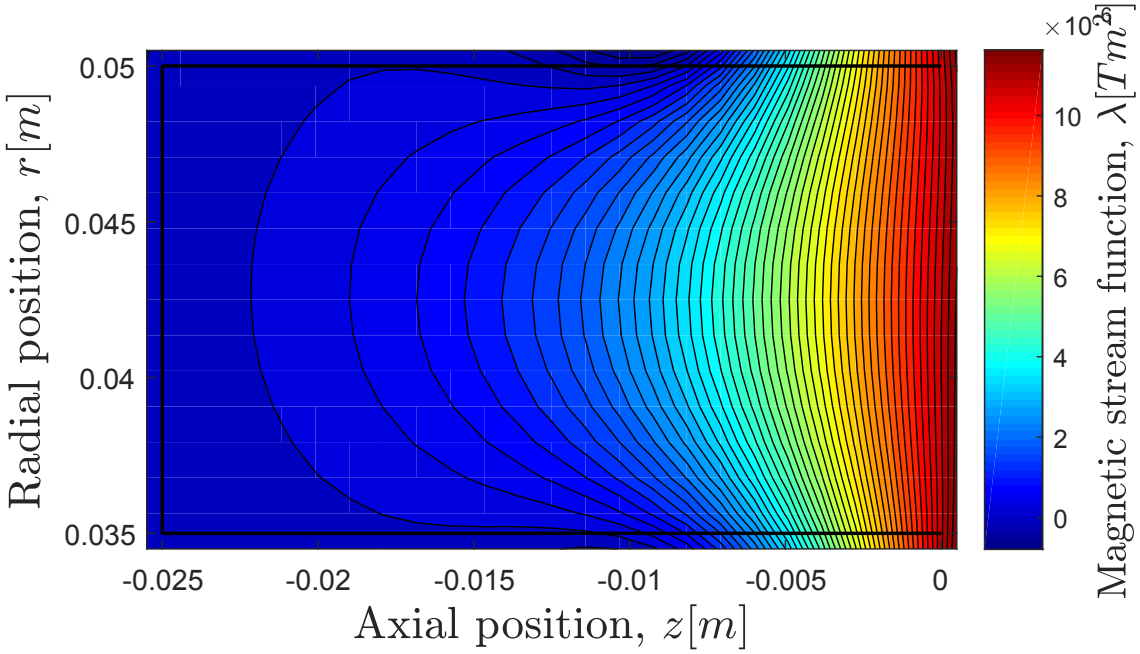

Figure 3.15: Magnetic streamlines in the discharge channel in MS topography

It is worth noting that an exhaustive iterative process was required to obtain the MS topography while maintaining a reasonable field intensity and fulfilling all coil requirements. To attain a better wall shielding (streamlines parallel to channel) and magnetic lensing (stronger bending in streamlines at the exit of the channel), it is necessary to extend the screens axially, but this simultaneously causes the magnetic field intensity to drop, as can be observed by comparison of Fig. 3.9b and Fig. 3.14b. Therefore, it is concluded that having lines practically parallel to walls inside the channel with a strong magnetic lensing at the exit may result inefficient if the corresponding strength of the magnetic field is extremely low, as will typically occur. For this reason, a trade-off between field intensity and the shape of the streamlines is needed, as it is the case in the topography achieved.

Whilst it may seem evident that the magnetic field intensity of a shielding topography can be ever increased by raising the different effective coil current intensities, the opposite is true. In the first place, reaching high NI will probably render the active elements infeasible to be manufactured. On the other hand, even if effective current could be raised largely, the impact on magnetic field intensity in the channel might be very small (especially close to the anode) provided the length of the screens is not reduced, given that the latter shield the channel. Furthermore, it should be noted that the required power input grows with the square of the effective current (3.8). In the end, a slight increase in field intensity may require a notable rise of coils' NI, which implies a large amount of additional power.

3.7 Design of a low-power Hall thruster

To conclude the studies on HETs, a small, low-power thruster will be designed on the basis of the SPT-100. The main parameters of the device will be computed by means of scaling laws, and, afterwards, the magnetic circuit will be designed accordingly.

3.7.1 Thruster sizing

Thanks to scaling laws, it is possible to attain relevant parameters of a thruster with a certain goal discharge power by sizing it down from data of a similar thruster (in this case larger and discharging at a higher power).

Within this strategy, the radial scaling [23] will be used to design a HET with discharge power $P_d = 200\ W$. The central idea is to attempt at maintaining the conditions of the plasma in the channel, i.e. density and temperature, with respect to the base thruster. In this line, the discharge voltage is kept constant while modifying the gas flow to control discharge power. Axial geometric parameters remain unchanged as well; the density of the plasma is conserved by changing those radial.

In accordance with this approach, input discharge variables (discharge voltage, maximum magnetic field intensity, channel length, thruster length, anode mass flow, channel width, channel mean radius, thruster radius) are related to P_d by the following laws, respectively

$$V_d, B_{max}, L_c, L_t = const \quad ; \quad \dot{m}_a \propto P_d \quad ; \quad h_c, r_c, R_t \propto P_d^{1/2} \tag{3.11}$$

whereas output discharge parameters (specific impulse, power input to magnetic circuit, plasma-wall interaction power loss, discharge current, thrust) accordingly fulfil

$$I_{sp} \propto const \quad ; \quad P_{mag} \propto P_d^{1/6} \quad ; \quad P_{wall} \propto P_d^{1/2} \quad ; \quad I_d, F \propto P_d \tag{3.12}$$

Therefore, the ratio of scaled thruster to the SPT-100 of any parameter ϕ, π_ϕ, is equal to the corresponding proportionality law among the previous. For instance, from eq. (3.12)

$$\pi_F = \frac{F_{scaled}}{F_{SPT-100}} = \frac{P_{d,scaled}}{P_{d,SPT-100}} = \pi_{P_d}$$

from which, evidently

$$F_{scaled} = \pi_F F_{SPT-100}$$

The process applies for any parameter above.

Furthermore, the total thruster efficiency can be computed from [4]

$$\eta_T = \frac{1}{2}\frac{F^2}{\dot{m}_a P_d}\eta_c \eta_o \tag{3.13}$$

where

$$\eta_c = \frac{\dot{m}_a}{\dot{m}_a + \dot{m}_c} \tag{3.14}$$

$$\eta_o = \frac{P_d}{P_d + P_k + P_{mag}} \tag{3.15}$$

are the cathode and electrical utilisation efficiencies, respectively. Note that the cathode keeper power, P_k is commonly null during operation [4], $P_k \approx 0$.

The cathode efficiency is opted to be similar in the scaled thruster, $\eta_{c,scaled} = \eta_{c,SPT-100}$, and the electrical utilisation efficiency can be computed with $P_{d,scaled}$ and $P_{mag,scaled}$ from scaling laws, thence giving the total thruster efficiency.

Data of the SPT-100 is gathered from [17], [24], [25] in Table 3.7, from which it is possible to obtain the corresponding parameters for the scaled-down thruster (shown in Table 3.8).

Parameter	**Value**
Discharge power, P_d [W]	1500
Discharge voltage, V_d [V]	300
Discharge current, I_d [A]	5
Anode mass flow, $\dot{m}_a$ [mg/s]	5.62
Cathode mass flow, $\dot{m}_c$ [mg/s]	0.5
Channel length, L_c [mm]	25
Channel width, h_c [mm]	15
Channel mean radius, r_c [mm]	42.5
Thruster length, L_t [mm]	50
Thruster radius, R_t [mm]	80
Maximum magnetic field intensity (channel), B_{max} [G]	250
Power input to magnetic circuit, P_{mag} [W]	34.6
Plasma-wall interaction power loss, P_{wall} [W]	225
Specific impulse, I_{sp} [s]	1590
Thrust, F [mN]	95.4
Thruster efficiency, η_T	0.496

Table 3.7: SPT-100 data

Parameter	Value
Discharge power, P_d [W]	200
Discharge voltage, V_d [V]	300
Discharge current, I_d [A]	0.67
Anode mass flow, $\dot{m}_a$ [mg/s]	0.75
Channel length, L_c [mm]	25
Channel width, h_c [mm]	5.5
Channel mean radius, r_c [mm]	15.5
Thruster length, L_t [mm]	50
Thruster radius, R_t [mm]	29.2
Maximum magnetic field intensity (channel), B_{max} [G]	250
Power input to magnetic circuit, P_{mag} [W]	28.2
Plasma-wall interaction power loss, P_{wall} [W]	82.2
Specific impulse, I_{sp} [s]	1590
Thrust, F [mN]	12.7
Thruster efficiency, η_T	0.434

Table 3.8: Scaled-down low-power Hall thruster parameters

3.7.2 Magnetic circuit

Given the parameters of the scaled thruster, collected in Table 3.8, it is possible to design a magnetic circuit complying with them. Therefore, the objective is to attain a combination of elements and properties that produce $B_{max} \approx 250\ G$ in the mean line of the new channel with a required power input of $P_{mag} = 28.2\ W$ (or less).

From the previous sizing, thruster and channel dimensions are known. For the purpose of attaining a magnetic topology akin to that of the reference case (which is in fact similar to the SPT-100, from which scaling-down is performed), the strategy to follow is in accordance with the radial approach. All parameters related to radial coordinates will follow the identical law used for scaling the thruster and mean-line channel radii (3.11), that is

$$\rho^{(i)} \propto P_d^{1/2} \tag{3.16}$$

for any element i in the circuit, and where ρ represents any of r_{min}, Δr. Therefore, using ratios of parameters as previously, and accounting for the difference in thruster radius between the reference case and the SPT-100 ($R_{t,ref} = 85\ mm$,

$R_{t,SPT-100} = 80\ mm$)

$$\frac{\rho^{(i)}}{\rho^{(i)}_{ref}} = \frac{\rho^{(i)}}{\rho^{(i)}_{SPT-100}} \frac{\rho^{(i)}_{SPT-100}}{\rho^{(i)}_{ref}} = \left(\frac{P_d}{P_{d,SPT-100}} \right)^{1/2} \frac{R_{t,SPT-100}}{R_{t,ref}} \tag{3.17}$$

Ultimately,

$$r^{(i)}_{min} = \sqrt{\frac{200}{1500}} \cdot \frac{80}{85} \cdot r^{(i)}_{min,ref}$$

$$\Delta r^{(i)} = \sqrt{\frac{200}{1500}} \cdot \frac{80}{85} \cdot \Delta r^{(i)}_{ref}$$

On the other hand, in consistency with the radial scaling method, axial parameters will remain essentially unchanged with respect to the reference case

$$\zeta^{(i)} \approx const \tag{3.18}$$

for any element i in the circuit, and where ζ represents any of z_{min}, Δz. A positive axial offset of 4 mm is introduced to the appropriate elements given that $L_{t,ref} = 54\ mm$, $L_{t,SPT-100} = 50\ mm$.

The resulting magnetic circuit and characteristics are displayed in Fig. 3.16. For the scaled thruster, it is necessary a power input of $P_{mag} = 6.3\ W$, which is notably lower than the value expected from the radial scaling (28.2 W), partially justified by the coil parametric study.

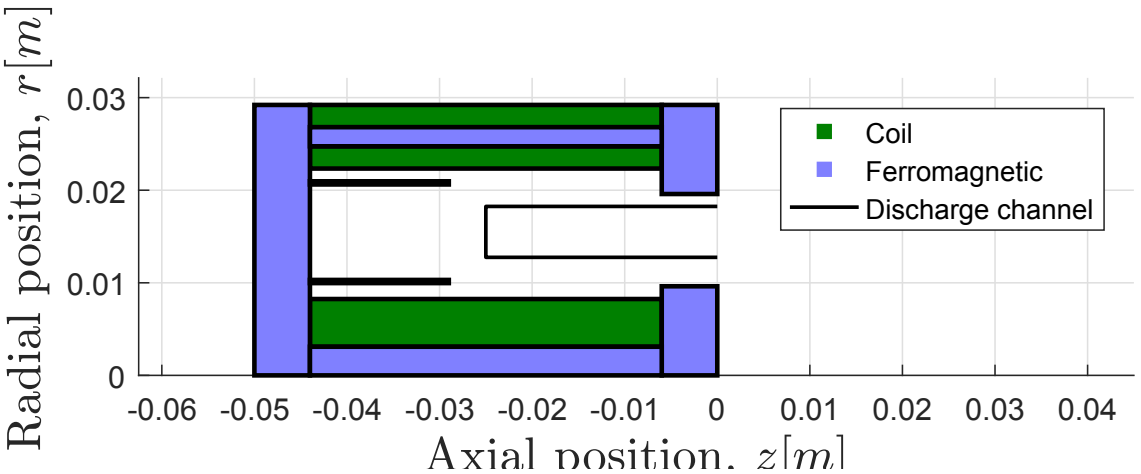

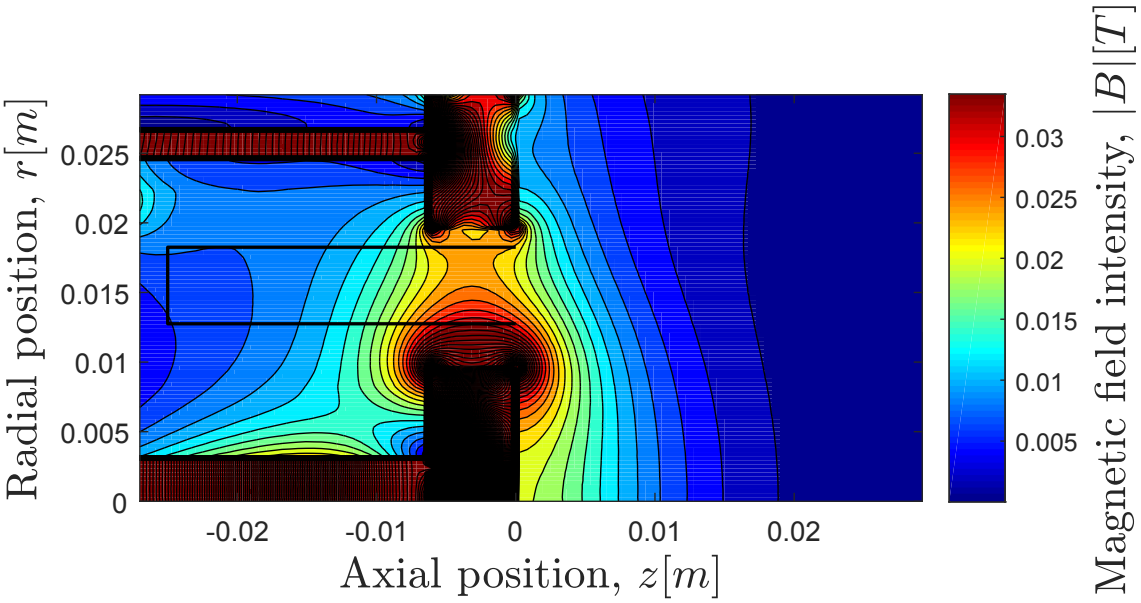

(b) Magnetic field intensity

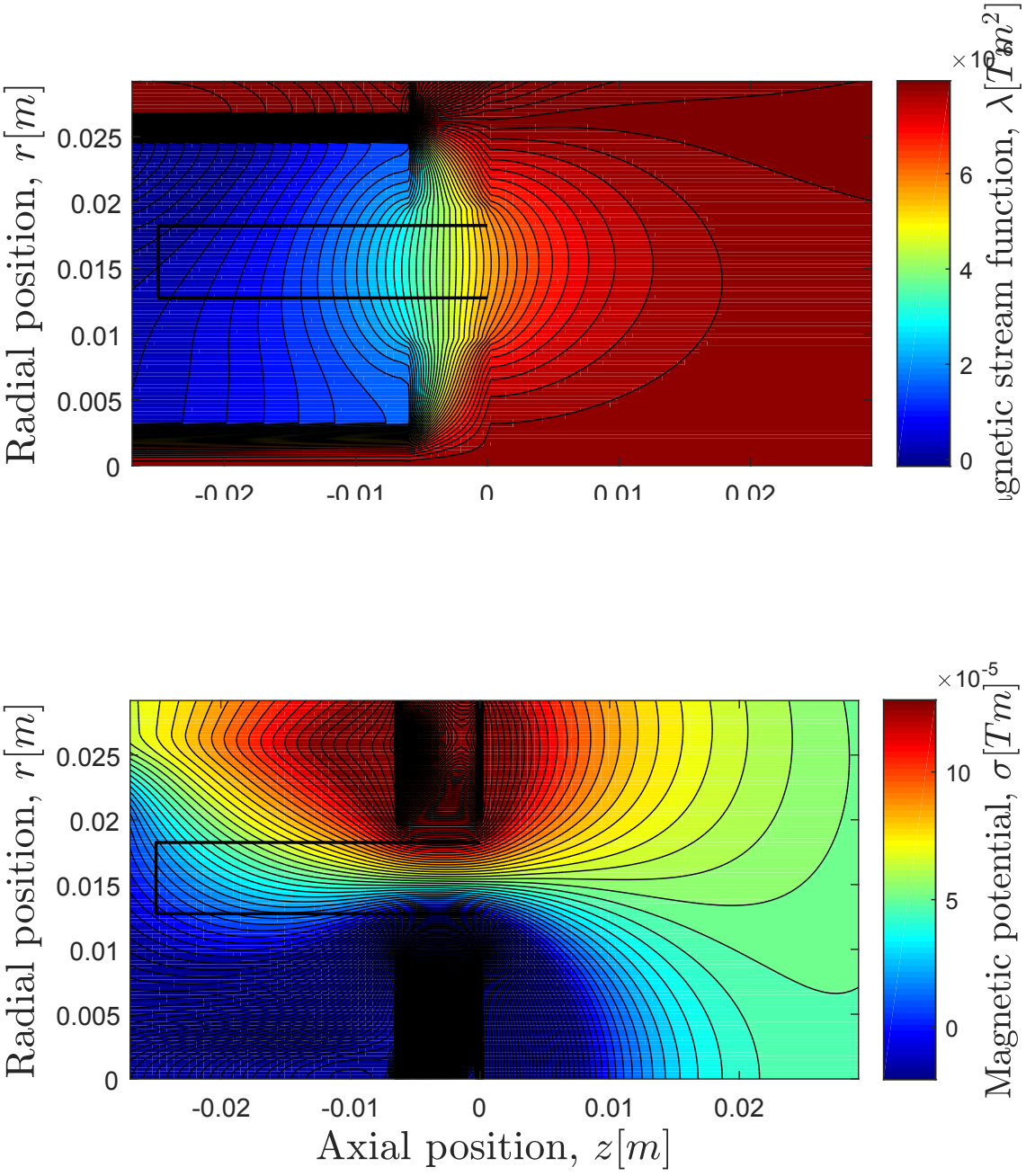

(d) Magnetic potential

Figure 3.16: Low-power scaled-down HET topography

Chapter 4

Socio-economic analysis

4.1 Thesis elaboration budget

Given that the present project is fundamentally theoretical, there is no cost associated to materials or experimental activities. The economic sources contributing to the elaboration budget are

- Software and licenses acquisition, C_{sw}
- Computer amortisation, A_{PC}
- Engineering cost (wage), C_{eng}

The total cost for elaborating the thesis is, thence

$$C_T = C_{sw} + A_{PC} + C_{eng} \tag{4.1}$$

In the first place, the cost related to software will be addressed. As mentioned in Chap. 2, the FEMM solver is open-source. Therefore, it is only necessary to account for the MATLAB license. The price for the version used, MATLAB R2016b amounts for the total software cost, and can vary depending upon the toolboxes included. A student license with the necessary packages accounts for

$$C_{sw} = 69 \text{ €}$$

On the other hand, amortisation of the laptop used can be computed from its original price, $P_{PC} = 269$ €. With an estimated lifetime $t_{PC,life}$ of 6 years, assuming

it will not be sold afterwards and noting that the elaboration of the thesis spanned ($t_{th,span}$) for 6 months

$$A_{PC} = P_{PC}\frac{t_{th,span}}{t_{PC,life}} = 269\ € \frac{6\ months}{6\ years \cdot 12\ months/year} = 22.4€$$

Finally, the engineering cost can be obtained considering the time investment on the elaboration of the project, $t_{th,elab} = 430\ h$, and assuming an undergraduate engineer wage of $W_{eng} = 10\ €/h$

$$C_{eng} = W_{eng} t_{th,elab} = 4300\ €$$

Therefore, the total cost of the project is (4.1)

$$C_T = 4391.4\ €$$

4.2 Socio-economic impact of the project

The repercussion of this thesis is essentially on research activities related to plasma thrusters. Possible scenarios include the social and/or economic outcome corresponding to the development of scientific papers, thruster prototypes, etc., whose detailed estimation is a priori unpredictable. As aforementioned in Sec. 2.5.4, the tool developed may become part of or be used along with HYPHEN, thus having an impact on any issue related to the simulation platform.

Chapter 5

Conclusion

Throughout the present project, insight into the effect of the different elements in a magnetic circuit has been provided. The parametric study on coil parameters renders the design of the magnetic circuit a process oriented towards element manufacturability and power-mass optimisation.

Design and modelling of relevant magnetic topographies was performed. Thanks to the tool developed and the FEMM solver, it was possible to carry out several simulations in short periods of time, allowing for the launching of batches and the use of the trial-and-error method.

On the other hand, an SPT-100-like Hall thruster was developed through the use of radial scaling laws. This approach allows to effectively size a new thruster from an existing one in a simple fashion.

In conclusion, it has been possible to develop a versatile magnetostatics simulation tool for axisymmetric thrusters with the capability to attain the magnetic characteristics of a given circuit, and with the possibility of working with a physics code for the purpose of simulating plasma thrusters. The coil design parametric study included in the code allows to decide on mass or power optimisation, or a trade-off between them, according to the needs of the user. Furthermore, given the inverse nature of the thruster problem, the use of the tool alongside an automatised magnetic mesher could allow for launching batches of simulations to adjust the final design of the device and observing the real effect of the topography on the efficiency of the thruster.

Building on the basis of the present thesis, additional future work may include the transition from the 2D axisymmetric model used throughout the project to a real three-dimensional thruster, and possibly the manufacture and testing of a prototype.

Acknowledgements

In the first place, I wish to express my sincere thanks to my tutor, Daniel Pérez, for his splendid guidance and unceasing support throughout the development of this project. Working with him has been a real pleasure for me, he has encouraged and guided me with vocation, patience and dedication. The knowledge I have acquired on electric propulsion and Hall thrusters, and the related enthusiasm I have about them I greatly owe to him.

Secondly, I am grateful to the Space Propulsion and Plasmas research group at UC3M, in particular to Pablo Fajardo and Eduardo Ahedo, for their valuable advice and for giving me the opportunity to collaborate with them.

On the other hand, I place on record my deep gratitude to Javier Rodríguez, from the Fluid Mechanics group, and Gonzalo Sánchez, Stefano Discetti and Andrea Ianiro, from the Aerospace Engineering group, for their inspiration, encouragement and outstanding teaching. I am indebted to them for much of what I have learned throughout my time at the university, and I greatly appreciate their influence on my academic trajectory.

Finally, I must express my gratitude to my partner for her constant support and encouragement towards progressing on my bachelor and thesis research, as well as for highly valuing my work and the effort behind it. I also thank my family and friends for their cheerfulness throughout my studies.

Bibliography

[1] Elise F. Morgan, Mary L. Bouxsein. (2005, December) Use of finite element analysis to assess bone strength. [Online]. Available: http://www.nature.com/bonekey/knowledgeenvironment/2005/0512/bonekey20050187/full/bonekey20050187.html

[2] Richard R. Hofer, "Development and Characterization of High-Efficiency, High-Specific Impulse Xenon Hall Thrusters," Ph.D. dissertation, University of Michigan, 2004.

[3] Steven Errede, Department of Physics, University of Illinois at Urbana-Champaign, "American Wire Gauge (AWG) & Metric Gauge Wire Sizes," UIUC Physics 436 EM Fields & Sources II, 2015.

[4] Dan M. Goebel, Ira Katz, *Fundamentals of Electric Propulsion: Ion and Hall Thrusters*, Joseph H. Yuen, Ed. Jet Propulsion Laboratory, California Institute of Technology, March 2008.

[5] James S. Sovey, Vincent K. Rawlin, Michael J Patterson, "Ion Propulsion Development Projects in US: Space Electric Rocket Test I to Deep Space 1," *Journal of Propulsion and Power*, vol. 17, no. 3, pp. 517–526, May-June 2001.

[6] Andrew Wilson, ESA Publications Division, "ESA Achievements (3rd edition)," European Space Agency, 2005.

[7] Marc D. Rayman, David H. Lehman, "Deep Space One: NASA's first Deep-Space technology validation mission," *Acta Astronautica*, vol. 41, no. 4, pp. 289–299, 1997.

[8] Mark R. Drinkwater, R. Haagmans, D. Muzi, A. Popescu, R. Floberghagen, M. Kern, M. Fehringer, "The GOCE gravity mission: ESA's first Core Earth Explorer," in *3rd International GOCE User Workshop*. ESA Special Publication, November 2006, pp. 1–8.

[9] Giulia Lecarrié. (2013, August) *Four Snecma plasma thrusters now in*

operation on Alphasat satellite. Safran Aircraft Engines.

[10] ——. (2016, January) *Snecma's PPS® 5000 plasma thruster selected for Neosat*. Safran Aircraft Engines.

[11] Richard R. Hofer et al., "The 12.5 kW Hall Effect Rocket with Magnetic Shielding (HERMeS) for the Asteroid Redirect Robotic Mission." 52nd AIAA/SAE/ASEE Joint Propulsion Conference, AIAA Propulsion and Energy Forum, 2016.

[12] United Nations Office for Outer Space Affairs, "United Nations Treaties and Principles on Outer Space, including related General Assembly resolutions and other documents," http://www.unoosa.org/res/oosadoc/data/documents/2013/stspace/stspace61_0_html/st_space_61E.pdf, 2013.

[13] D. C. Meeker, "Finite Element Method Magnetics Version 4.2 (12Jan2016 Build)," http://www.femm.info/wiki/HomePage.

[14] ——, *Finite Element Method Magnetics User Manual*, Version 4.2, October 2015.

[15] B. D. Cullity, C. D. Graham, *Introduction to Magnetic Materials*, 2nd ed. John Wiley & Sons, 2008.

[16] Jean-Pierre Boeuf, "Tutorial: Physics and modeling of Hall thrusters," *Journal of Applied Physics*, vol. 121, no. 1, January 2017.

[17] Eduardo Ahedo, Pablo Fajardo, Daniel Pérez Grande, "Evaluation of Erosion Reduction Mechanisms in Hall Effect Thrusters." Joint Conference of 30th International Symposium on Space Technology and Science, 34th International Electric Propulsion Conference and 6th Nano-satellite Symposium, July 2015.

[18] R. A. Matula, Center for Information and Numerical Data Analysis and Synthesis, Purdue University, "Electrical Resistivity of Copper, Gold, Palladium, and Silver," J. Phys. Chem. Ref. Data, Vol. 8, No 4, 1979.

[19] P. Renaudin et al., "Magnetic circuits for Hall thrusters: use of permanent magnets," Groupement de Recherche CNRS / CNES / SNECMA / ONERA no. 2232 "Propulsion Plasmique pour Systèmes Spatiaux".

[20] L. Garrigues et al., "Model study of the influence of the magnetic field configuration on the performance and lifetime of a Hall thruster," *American Institute of Physics*, vol. 10, no. 12, September 2003.

[21] Logan T. Williams, "Ion Acceleration Mechanisms of Helicon Thrusters ," Ph.D. dissertation, Georgia Institute of Technology, 2013.

[22] Ioannis G. Mikellides, Ira Katz, Richard R. Hofer, Dan M. Goebel, "Magnetic shielding of a laboratory Hall thruster. I. Theory and validation," *Journal of Applied Physics*, vol. 115, no. 4, January 2014.

[23] E. Ahedo, J. M. Gallardo, "Scaling down Hall thrusters," E.T.S.I. Aeronáuticos, Universidad Politécnica de Madrid, Spain, 2003.

[24] John M. Sankovic, John A. Hamley, Thomas W. Haag, "Performance Evaluation of the Russian SPT-100 Thruster at NASA LeRC," 23rd International Electric Propulsion Conference. Lewis Research Center, September 1993.

[25] K. Matyash et al., "Self consistent kinetic simulations of SPT and HEMP thrusters including the near-field plume region," December 2009.